PANA-GOESP-CR3

GOES D, E, F PROGRESS REPORT

ENERGETIC PARTICLE SENSOR DOME CALIBRATION WORK

Calibration Report
P.O. #08-779413-LBG

August 26, 1980

Prepared for

Hughes Aircraft Company
P.O. Box 92919
Los Angeles, CA 90009

by

PANAMETRICS, INC.
221 Crescent Street
Waltham, MA 02154

TABLE OF CONTENTS

LIST OF ILLUSTRATIONS (Cont'd)

LIST OF TABLES

LIST OF TABLES (Cont'd)

1. INTRODUCTION

1.1 Overview

This report provides a summary of the geometrical factor results for the GOES D, E & F Energetic Particle Sensor (EPS) DOME. This unit measures protons and alpha particles from approximately 15 MeV/nucleon to 500 MeV and electrons above 2 MeV. Because GOES is a geosynchronous orbit satellite, the particle flux consists essentially of that from solar proton events (in which the alpha particle intensity is generally a few percent of the proton intensity), superimposed upon a lower level of outer radiation belt trapped protons having insignificant intensity above a few MeV and trapped electrons having a moderate intensity of up to a few MeV. The DOME unit uses the same principle of shielding - determined energy thresholds as was used for the previous GOES and SMS satellites but differs in some significant design details. It was, therefore, decided that a program of engineering model calibration using particle accelerators and radioactive sources would be carried out in order to determine the variation of geometrical factors with incident particle energy and angle for protons, and to determine the effective threshold energy for electrons.

There are two types of geometrical factors of interest: that for the in-aperture particles in the relatively low energy range to be measured, and that for the high energy particles (essentially protons) that are capable of penetrating the DOME shielding and producing spurious counts.

Most of the data were taken at the Harvard Cyclotron which provides 160 MeV protons. By the use of absorbers, the proton energy could be degraded to below 20 MeV. Some additional lower energy proton data were taken at the Brookhaven National Laboratory on the Tandem Van de Graaff facility.

This first section of the report contains a brief design description, including a listing of the energy bins, and a summary of the accelerator data-taking operations. The second section of the report is devoted to the primary geometrical factor determinations, while the third gives details of spurious count results due to penetrating protons. The fourth section contains a brief summary of all results and some conclusions. Acknowledgements conclude the report.

1.2 Design Description

A cross section of the DOME assembly showing the three separate modules is given in Figure 1.1. The details of the detector assembly for the D3 (lowest energy) module are shown in Figure 1.2. The three DOME

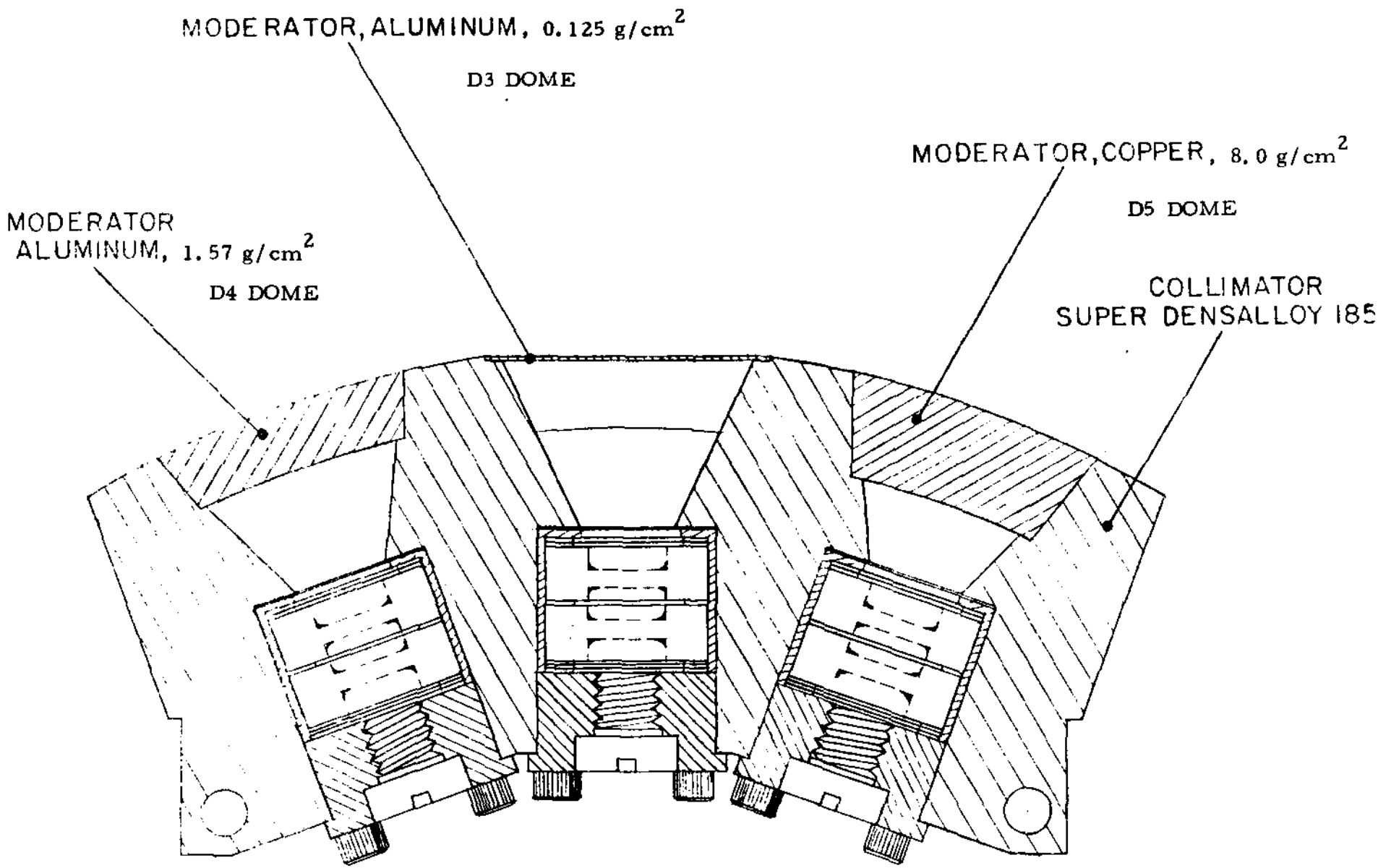

Figure 1.1 DOME Cross Section Showing the Three Separate Modules

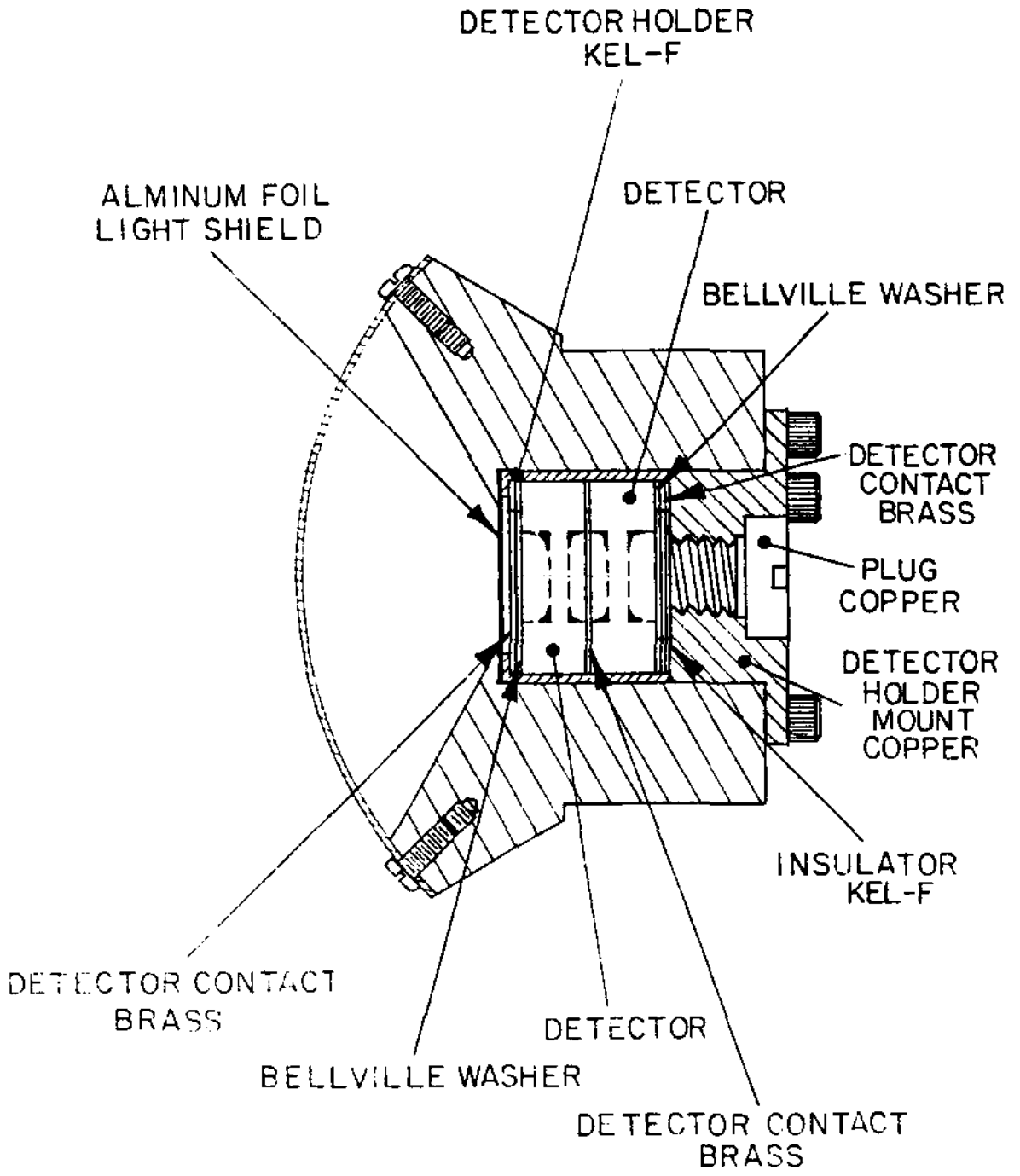

Figure 1.2 Cross Section of the D3 DOME Module, Showing the Detector Assembly Details

modules use a tungsten-base collimator to define the primary field-of-view, $\pm 60^{\circ}$ along the spin axis and $\pm 30^{\circ}$ in the spin plane. The tungsten collimator shields the detectors from protons below about 120 MeV. The detector modules consist of two 1500 μm thick, 25 mm^2 area, totally depleted Si surface barrier detectors, with a 0.145 mil Al foil light shield. The particle/energy bins are determined primarily by the moderator thicknesses and by energy thresholds for the detector pairs.

1.3 Energy Bin Definition

In order to define the energy/particle bins, it is necessary to calculate energy losses in the moderators and the two detectors for the types of particles of interest. Here we use the following expression for the stopping power:

$$S(E) = -dE/ds = \left(\frac{1}{kn}\right) (E + \epsilon)^{1-n} \qquad (1.1)$$

This is similar to the simple power law expression often used to approximate the stopping power, except that the constant ϵ is included. This causes S(E) to approach a constant, rather than infinity, as $E \longrightarrow 0$. Experimentally, it is found that S(E) peaks at a very low energy (~100 keV), but this is unimportant for present purposes because the range of protons and alphas ≤ 100 keV is small (≤ 1 μm Si).

By use of (1.1), it is simple to show that the average energy just necessary to pass through a pathlength s of any absorbing material, the so-called "range energy", is

$$E_r = (\epsilon^n + s/k)^{1/n} - \epsilon \qquad (1.2)$$

For particles of energy E less energy than E_r, on an average the entire energy E is deposited in the material. Thus, the deposited energy is exactly

$$E_{dep} = E, \qquad E \leq E_r \qquad (1.3)$$

For energies E greater than E_r, there are two cases that must be differentiated: small and large energy deposition. If E_{dep} is small, it is appropriate to use (1.1) directly. Thus, we use for the average energy deposition

$$E_{dep} = s\,S(E), \qquad s\,S(E)/E \leq .001, \quad E > E_r \qquad (1.4)$$

For larger energy deposition, we obtain by use of (1.1)

$$E_{dep} = (E + \epsilon) - \left[(E + \epsilon)^n - s/k\right]^{1/n}, \quad s\,S(E)/E > .001, \quad E > E_r \tag{1.5}$$

Equation (1.5) goes over into (1.4) in the case $(E + \epsilon)^n \gg s/k$, which is equivalent to $s\,S(E)/E \ll 1$. The choice of .001 as the dividing point between use of (1.4) and (1.5) is arbitrary. Equation (1.5) is analytically correct for all $E > E_r$, of course. However, for small energy depositions, it requires the computation of the difference between the two large numbers in order to obtain a small one. In that instance, it is computationally more accurate to use (1.4) directly. For particles incident at an angle θ from the normal to an absorber of thickness x, the pathlength s is

$$s = x/\cos\theta \tag{1.6}$$

Thus, to find an energy deposition for a particle of energy E incident at angle θ on an absorber (detector or foil) of thickness x, first calculate E_r from (1.2). If $E \leq E_r$, then use (1.3). Otherwise, calculate S(E) from (1.1). If $s\,S(E)/E \leq .001$, use (1.4); if not, use (1.5).

The constants ϵ, n and k depend upon the particle type, the absorber material, and the units used to describe particle energy and absorber thickness. The values used for protons and alpha particles are listed in Table 1.1. For silicon, the theoretical stopping power data fitted were taken from Ref. 1.1; for aluminum, the proton data were taken from Ref. 1.2, while the alpha particle data came from Ref. 1.3. For protons, the range of validity is 0.5 - 100 MeV; for alphas, it is 2 - 200 MeV. The fit on S(E) is within about $\pm 2\%$ in all cases; over most of the range of validity it is much better. For copper and the second set of aluminum data, the range of validity is 5 - 500 MeV and were used for the D4 and D5 calculations. For electrons in the D3 DOME, the energy losses were calculated by interpolation from the Range/Energy tables in Ref. 1.4 for aluminum and in Ref. 1.5 for silicon.

The detector thicknesses were measured using an x-ray absorption method developed at Panametrics (Ref. 1.6) and were all within 2% of the nominal 1500 μm. A total silicon detector thickness of 3000 μm was thus used with the above procedure to calculate the energy deposition (loss) for electrons, protons, and alpha particles, with the results plotted in Figures 1.3, 1.4, and 1.5 for the D3, D4, and D5 DOMES. As shown in the bottom of Figure 1.5, the detector separation is 5.6 mm (outer face separation)

TABLE 1.1

Energy Deposition Constants

Material	Units for s	For protons			For alphas		
		ϵ*	n	k	ϵ*	n	k
Aluminum	g/cm^2	0.257	1.781	0.002698	1.222	1.794	0.0002157
Silicon	microns	0.353	1.795	10.764	1.766	1.802	0.8665
Copper	g/cm^2	-8.535	1.571	0.009737	-34.52	1.570	0.001114
Aluminum**	g/cm^2	-8.871	1.582	0.007856	-0.436	1.762	0.0002581
Silicon**	microns	-8.830	1.582	32.840	-0.434	1.761	1.0901

*E and ϵ are in MeV

**For E>50 MeV

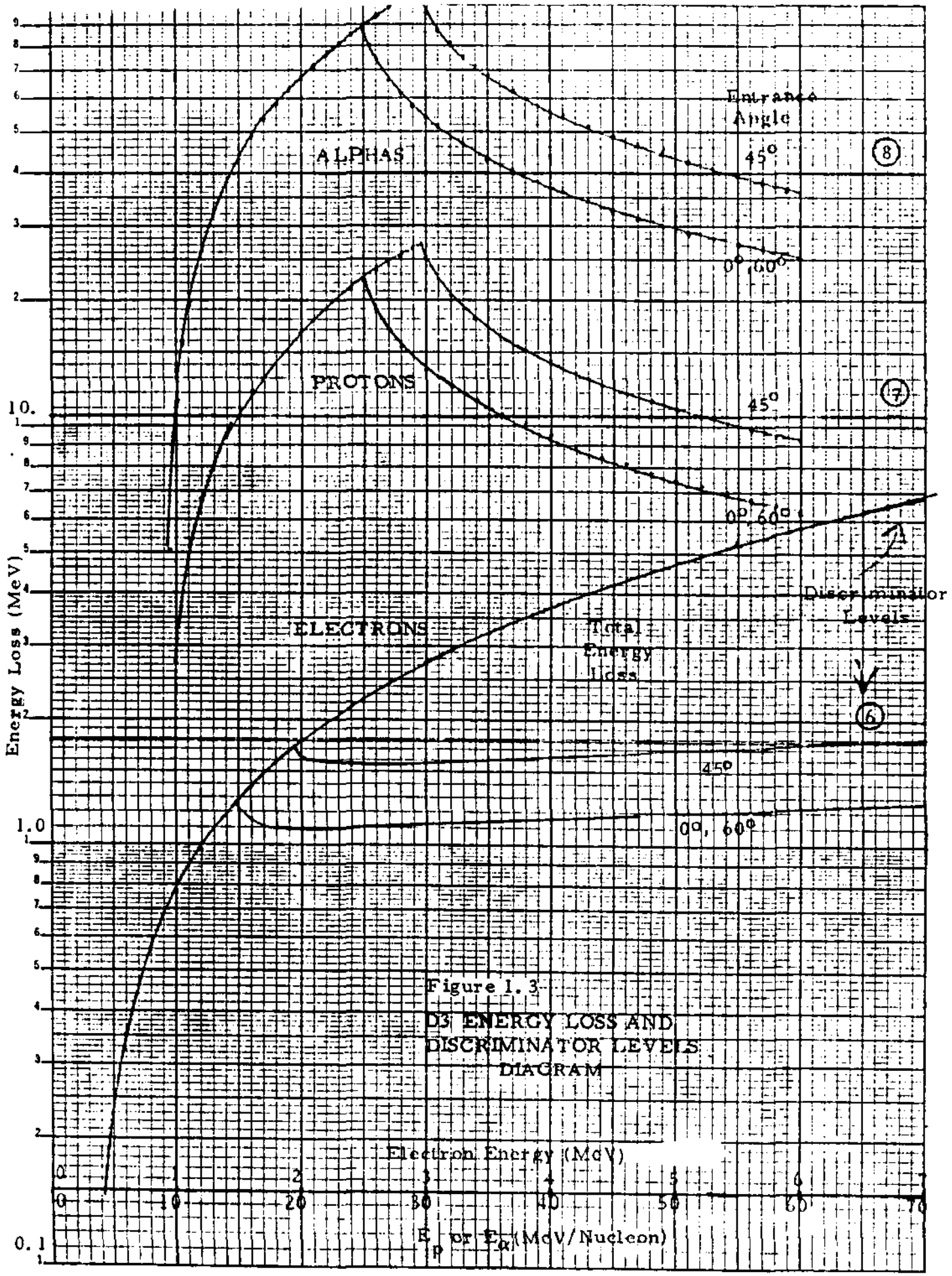

Figure 1.3
D3 ENERGY LOSS AND DISCRIMINATOR LEVELS DIAGRAM

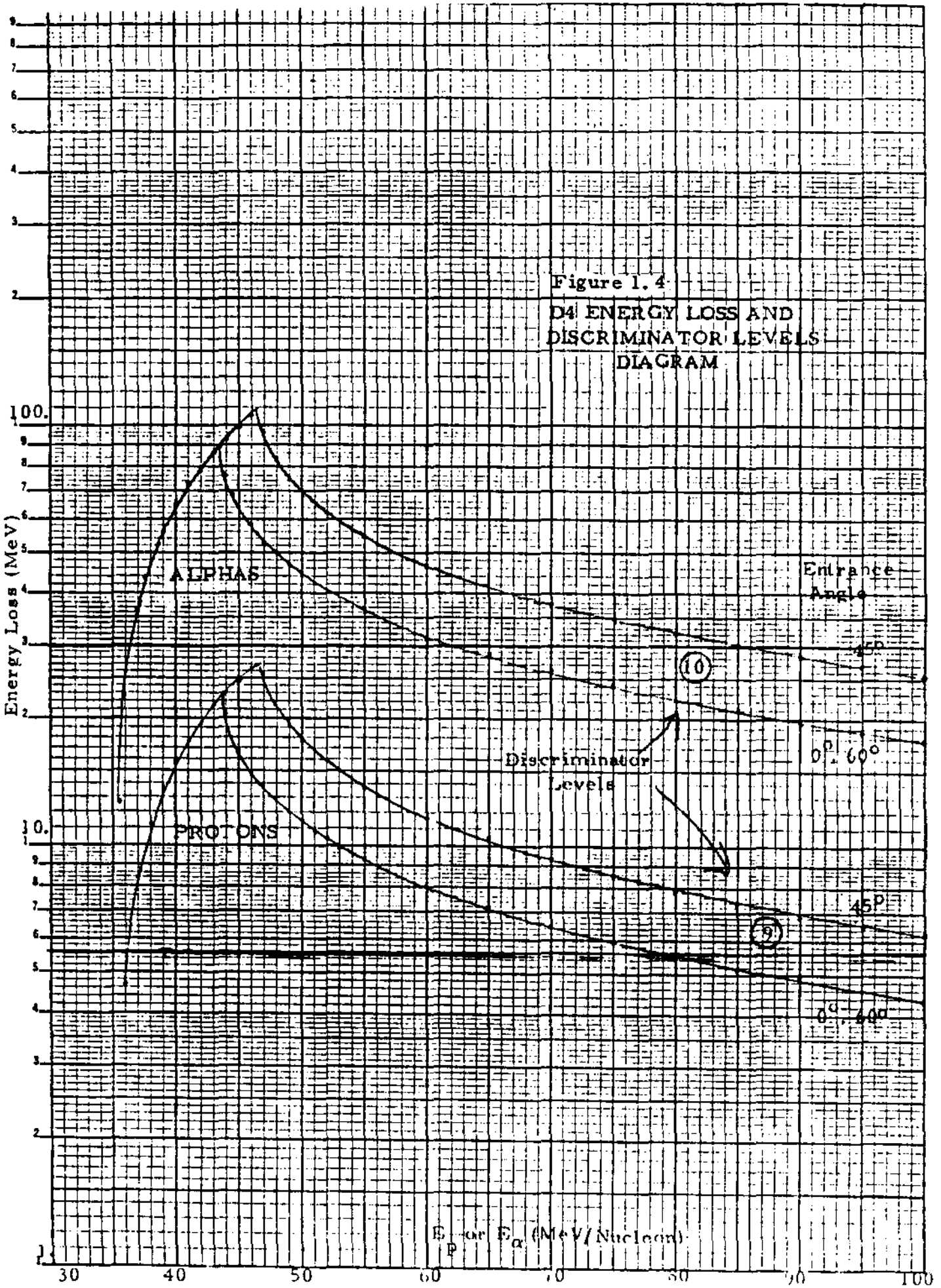

Figure 1.4

D4 ENERGY LOSS AND DISCRIMINATOR LEVELS DIAGRAM

Figure 1.5

D5 ENERGY LOSS AND DISCRIMINATOR LEVELS DIAGRAM

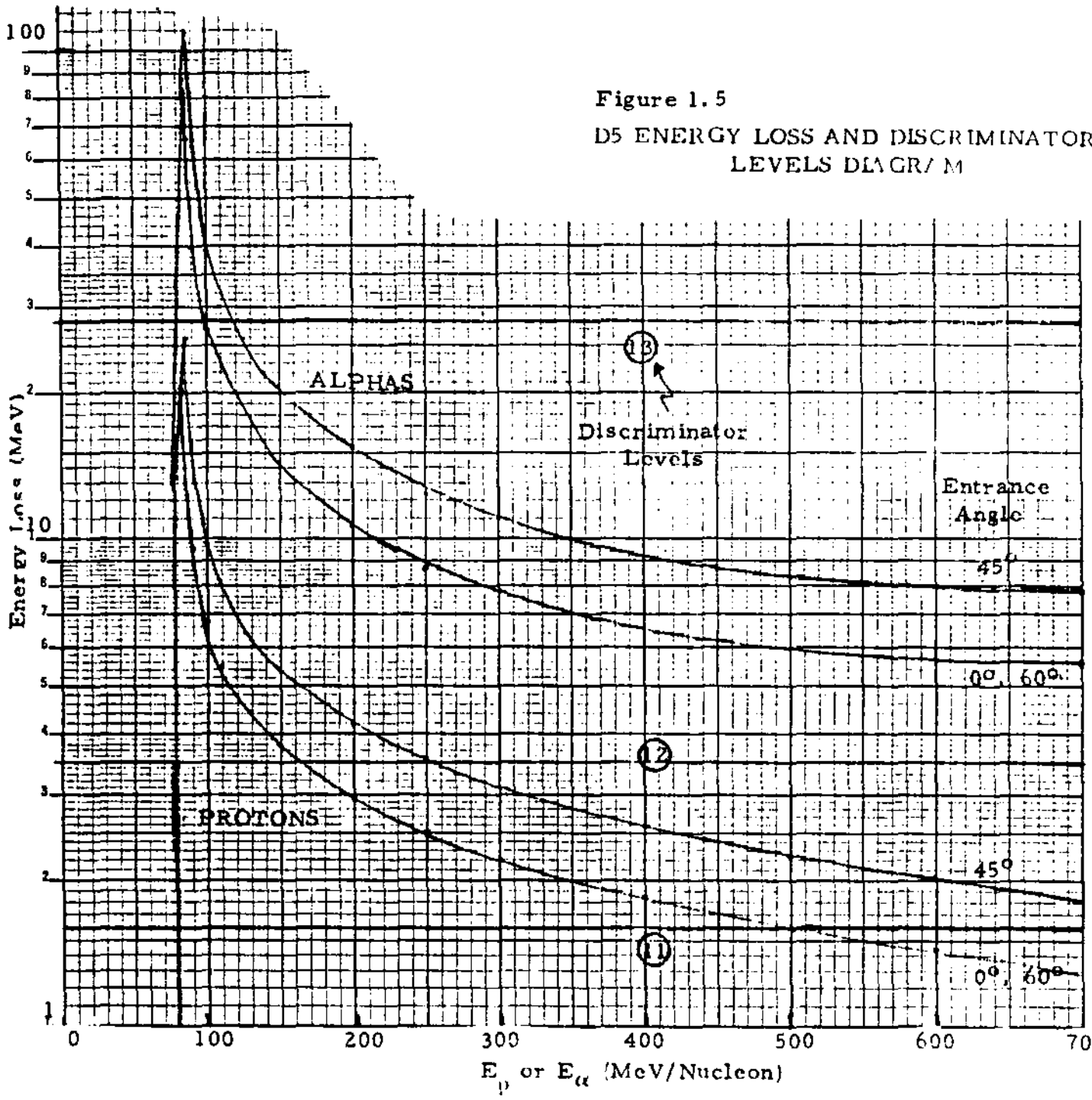

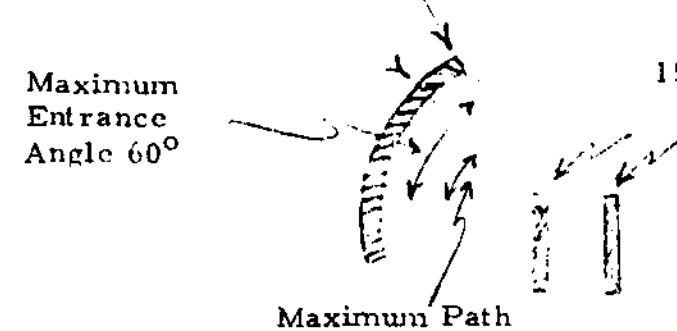

DOME ENERGY DEPOSITION CALCULATION DIAGRAM

so the maximum path length occurs at 45°, and the 60° path length is the same as for 0°. Two sets of curves are thus shown for (0°, 60°) and for (45°). The resulting energy detection ranges for the DOME are given in Table 1.2.

1.4 Experimental Observations Summary

1.4.1 Data Taking Periods

The primary data taking period for the DOME engineering model was July 18 to 21, 1978, at the Harvard Cyclotron. Some low energy proton data were also taken at the Brookhaven National Laboratory Tandem Van de Graaff during the telescope tests on July 25 to 27, 1978, (Refs. 1.7 - 1.9). Additional data were acquired at the Harvard Cyclotron with the Protoflight DOME on July 14 to 15, 1979, with the Flight One DOME on January 26 to 27, 1980, and with the Flight Two DOME on April 26, 1980.

1.4.2 Energy/Angles Used

The calibration of the SMS A, B, C and GOES B and C DOME Detectors is described in Refs. 1.10 and 1.11. The earlier design consisted of a 3 mm cubical lithium drifted silicon detector on a tungsten back shield, covered with a hemispherical absorber. The present design using totally depleted silicon surface barrier detectors is sufficiently different to warrant a complete calibration. An engineering model was calibrated extensively with the energy/angles covered being given in Table 1.3 for the high energy proton runs at the Harvard Cyclotron, and in Table 1.4 for some lower energy proton runs at the BNL Tandem Van de Graaff. Some minor changes were made in the tungsten shield design for the Protoflight and two Flight units; therefore, the Protoflight unit was rechecked with some detailed angle scanning at one energy for each of the three DOME detectors as shown in Table 1.5. All of the flight units (PF, F1 and F2) were calibrated over a broad set of energies for $(\theta/\phi) = (0/0)$ as shown in Tables 1.5 and 1.6.

The experimental setup at the Harvard Cyclotron is diagramed in Figure 1.6, while the setup at the BNL Tandem Van de Graaff is shown in Figure 1.7. Some pictures of the experimental setups are shown in Figure 1.8 for Harvard and in Figure 1.9 for BNL. A detailed close-up of the Telescope (Ref. 1.9) mounted on the rotating table at Harvard is shown in Figure 1.10.

All tests with the engineering model and Protoflight DOME units were made with the setups shown in Figures 1.6 and 1.7 (engineering model only). For the Flight One and Flight Two units, a second monitor detector

TABLE 1.2

DOME Energy Bin Limits

DOME Module	Threshold Level No.	Threshold Level (MeV)	Electron Range (MeV)	Proton Range (MeV) $(0^o, 60^o)$	Proton Range (MeV) (45^o)	Alpha Range (MeV) $(0^o, 60^o)$	Alpha Range (MeV) (45^o)
D3	L6	1.77	2 - ∞	9.6-380	9.6- ∞	37- ∞	37- ∞
D3	L7	10.5	-----	14.7-36.5	14.7-52	40-760	40-1400
D3	L8	40	-----	---	---	57-151	57-216
D4	L9	5.6	-----	36.3-79	36.3-109	141-2700	141- ∞
D4	L10	30	-----	---	---	146-252	146-342
D5	L11	1.6	-----	80-500	80- ∞	320- ∞	320- ∞
D5	L12	3.5	-----	80-165	80-256	320- ∞	320- ∞
D5	L13	28	-----	---	---	321-397	321-483

Energy Bin	Logic	Electron Range (MeV)	Proton Range (MeV)	Alpha Range (MeV)
E1	$6 \cdot \overline{7}$	2 - ∞	9.6 - (380, ∞)	(----)
P4	$7 \cdot \overline{8}$	-----	14.7 - (36.5, 52)	(----)
A4	8	-----	----	57 - (151, 216)
P5	$9 \cdot \overline{10}$	-----	36.3 - (79, 109)	(----)
A5	10	-----	----	146 - (252, 342)
P6	$12 \cdot \overline{13}$	-----	80 - (165, 256)	(----)
P7	$11 \cdot \overline{12}$	-----	(165, 256)-(500, ∞)	(----)
A6	13	-----	----	321 - (397, 483)

Table 1.3

EPS DOME Detector Runs Taken at the Harvard Cyclotron

E_p (MeV)	Front Rear	θ/ϕ angles covered - D3 DOME Detector				
144	F	0/0, 30, 45, 60, 75, 90	15/0	30/0, 30	45/0	
	R	0, 30, 60/180				
108	F	0/0, 30, 45, 60, 75, 90	15/0	30/0, 30	45/0	60/0
	R	0, 30, 60/180				
94	R	0, 30, 60/180				
79	F	0/0, 30, 45, 60, 75, 90	15/0	30/0, 30	45/0	
	R	0, 30, 60/180				
60	F	0/0, 30, 45, 60	15/0	30/0, 30	45/0	60/0
45	F	0/0, 30, 45, 60	15/0	30/0, 30	45/0	60/0
33	F	0/0, 30, 45, 60	15/0	30/0, 30	45/0	60/0
	F		-15/0	-30/0		

E_p (MeV)	Front Rear	θ/ϕ angles covered - D4 DOME Detector				
153	F	0/0				
	R	0, -30, -60/180				
138	R	0, -30, -60/180				
119	F	0/0				
	R	0, -30, -60/180				
106	F	0/0				
	R	0, -30, -60/180				
96	R	0, -30, -60/180				
92	F	0/0				
	R	0, -30, -60/180				
82	F	0/0				
76	F	0/0				
69	F	0/0				
64	F	0/0				
55	F	0, ±15, ±30, ±45, 60/0				
144	F	0/0,15,30,45,60,75,90	-15/0,30	-30/0, 30	-45/0,30	-60/0,30
108	F	0/0,15,30,45,60,75,90	-15/0,30	-30/0, 30	-45/0,30	-60/30
133	F	0/0				
79	F	0/0,15,30,45,60,75,90	-15/0,30	-30/0, 30	-45/0,30	-60/30
67	F	0/0				
60	F	0/0, 15, 30, 45, 60, 75	-15/0,30	-30/0, 30	-45/0,30	-60/30
45	F	0/0, 15, 30, 45, 60, 75	-15/0,30	-30/0, 30	-45/0,30	
52	F	0/0				
33	F	0/0, 15, 30, 45, 60	-15/0,30	-30/0, 30	-45/30	
	F	15, 30, 45, 60, /0				

Table 1.3 (cont'd)

E_p (MeV)	Front Rear	θ/φ angles covered - D5 DOME Detector				
153	F	0/15, 30, 45, 60, 75, 90	-15/30,60	-30/30,60	-45/30,60	-60/30,60
	R	0, -30, -60/180				
138	F	0/15, 30, 45, 60, 75, 90	-15/30,60	-30/30,60	-45/30,60	-60/30,60
	R	0, -30, -60/180				
131	F	0/15				
	R					
123	F	0/45, 60, 75				
	R					
119	F	0/15, 30, 45, 60, 75, 90	-15/30,60	-30/30,60	-45/30,60	-60/30
	R	0, -30, -60/180				
127	F	0/30, 90	-15/30	-30/30	-45/30	-60/30
	R					
106	F	0/15, 30, 45, 60, 75	-15/30,60	-30/30,60	-45/30,60	-60/30
	R	0, -30, -60/180				
97	F	0/15, 30, 45, 60	-15/30	-30/30	-45/30	
	R	0/180				
92	F	0/15/30, 45, 60	-15/30	-30/30	-45/30	
	R	0, -30, -60/180				
144	F	0, ±15, ±30, ±45, ±60/0				
133	F	0, ±15, ±30, ±45, ±60/0				
128	F	0, ±15, ±30, ±45, ±60/0				
121	F	0/0				
108	F	0, ±15, ±30, ±45, -60/0				
94	F	0, ±15, ±30, ±45/0				
84	F	0, -15, -30, -45/0				
79	F	0, -15, -30/0				
78	F	0, -15, -30, -45/0				

Table 1.4

DOME Detector D3 Runs with Protons at BNL (GOES-EPS)

Proton Energy (MeV)	θ angle range (deg) (mostly in 5° steps) ($\phi = 0$)
32.0	-15 to +50
29.0	-10 to +40
25.0	-10 to +10
20.0	-10 to +40
15.0	-10
12.0	-10 to +40

TABLE 1.5

EPS DOME Protoflight Unit Runs Taken at the Harvard Cyclotron

E_p (MeV)	θ/ϕ angles covered-PF S/N 001-D3 DOME Detector
66, 59, 51, 44, 38, 32, 30, 25, 17, 13	0/0
30	0/45
25	0, 15, 30/0, 15, 30, 45, 60
25	45/0, 15, 30

E_p (MeV)	θ/ϕ angles covered-PF S/N 001-D4 DOME Detector
144	0, $\pm$15, $\pm$30, 45/0
133, 128, 121, 111, 94, 84, 79, 66, 59, 51, 44, 38, 32, 30	0/0
44	0/45
51	0, 15, 30/0, 15, 30, 45, 60
51	45/0, 15, 30, 45

E_p (MeV)	θ/ϕ angles covered-PF S/N 001-D5 DOME Detector
144	0, $\pm$15, $\pm$30, $\pm$45/0
133, 128, 121, 111, 94, 84, 79	0/0
94	0, 15, 30/0, 15, 30, 45, 60
94	45/0, 15, 30

TABLE 1.6

EPS DOME Flight Unit Runs Taken at the Harvard Cyclotron

Flight-One S/N 002 and Flight-Two S/N 003 DOME data taken at $\theta/\phi = 0/0$

D3 DOME Detector data taken at E_p (MeV):

66, 59, 51, 44, 38, 32, 30, 25, 17, 13

D4 DOME Detector data taken at E_p (MeV):

121, 111, 94, 84, 79, 66, 59, 51, 44, 38, 32, 30

D5 DOME Detector data taken at E_p (MeV):

144, (S/N 003 only), 133, 128, 121, 111, 94, 84, 79

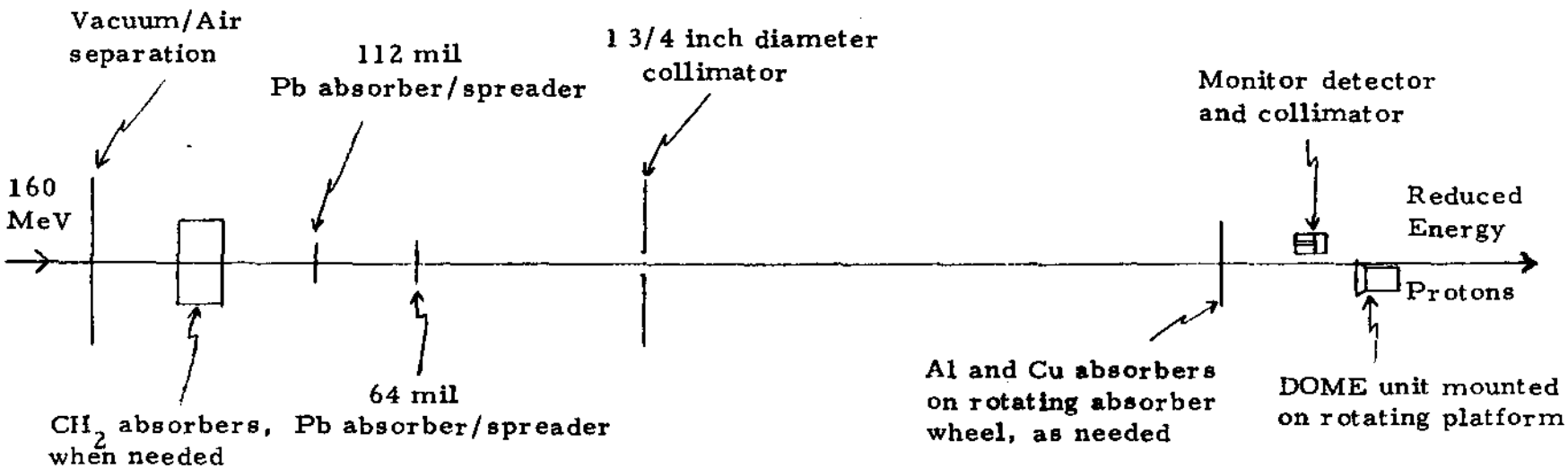

Figure 1.6 General Experimental Setup at the Harvard Cyclotron

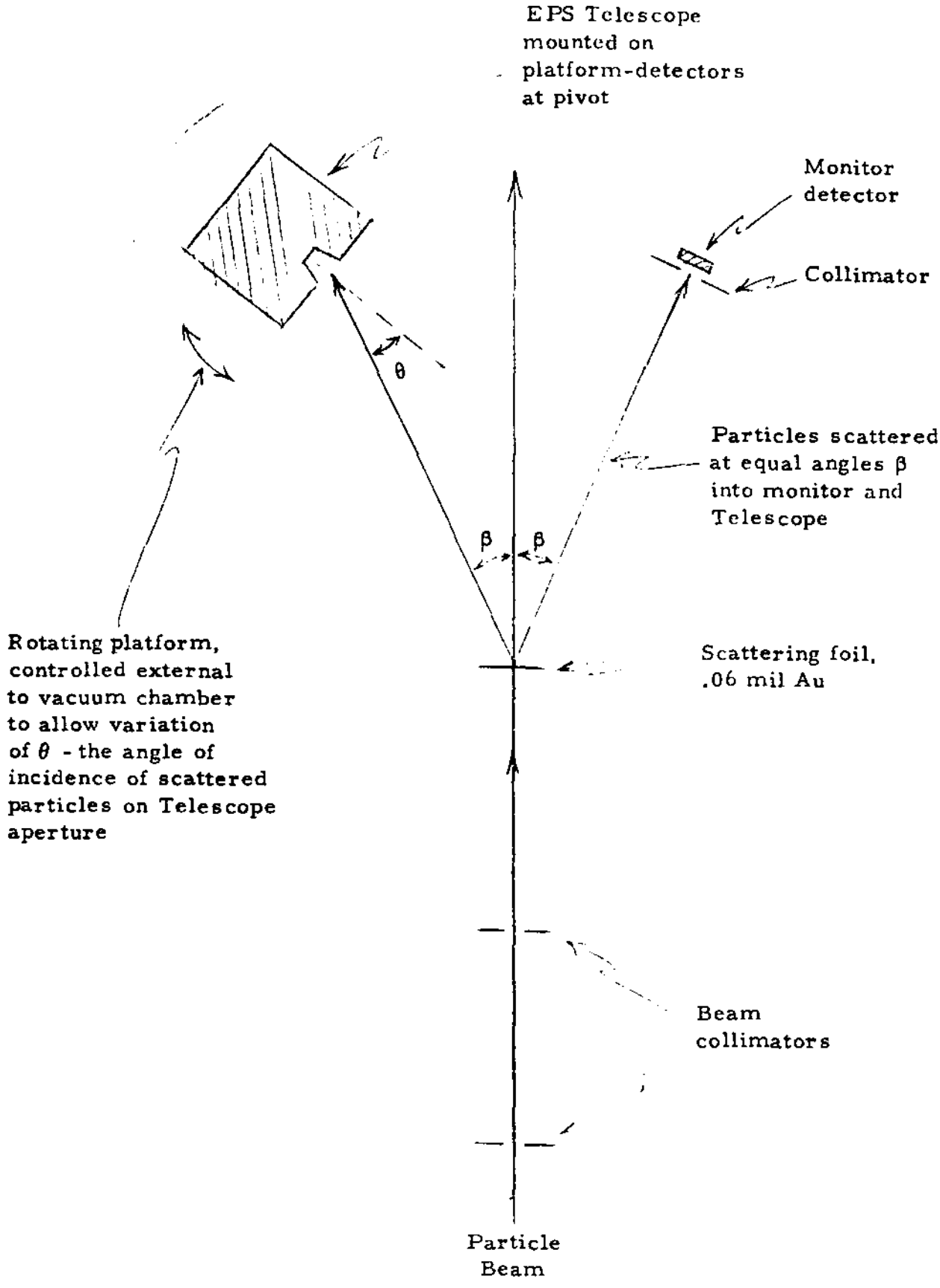

Figure 1.7 General Experimental Setup at Brookhaven National Laboratory

Fig. 1.8 SET UP AT HARVARD CYCLOTRON

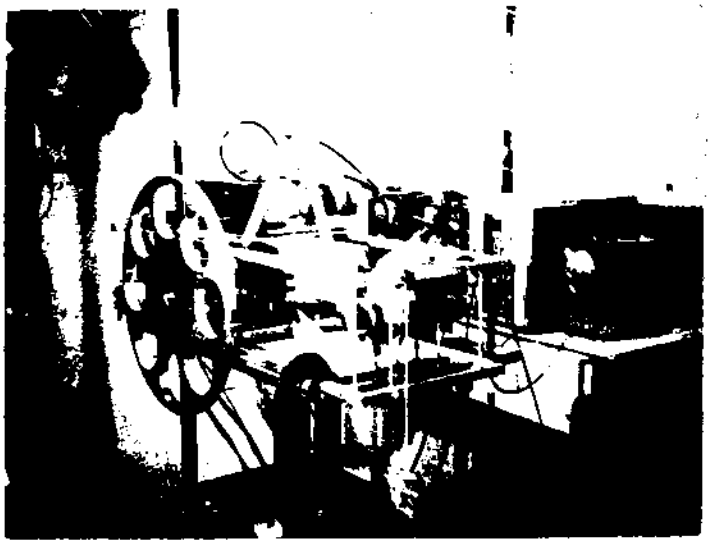

General set up showing wheel for mounting absorbers to vary incident energy.

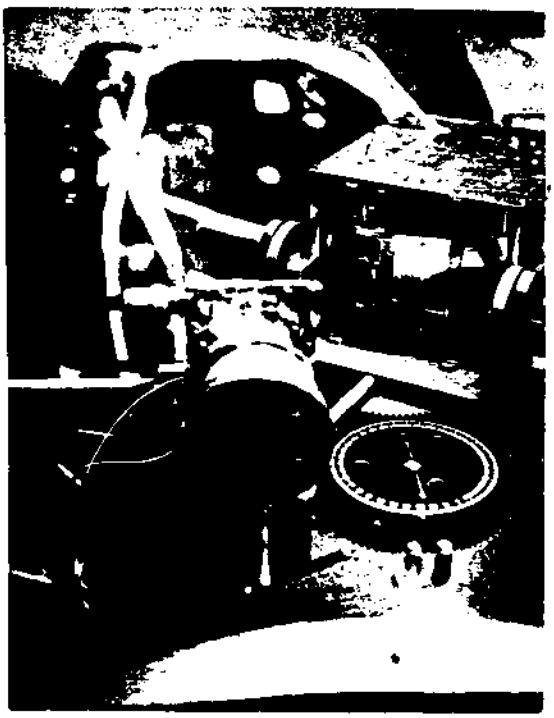

Beam Direction

Fixed monitor detector and Dome mounted on rotating assembly.

Fig. 1.9 SET UP AT BNL

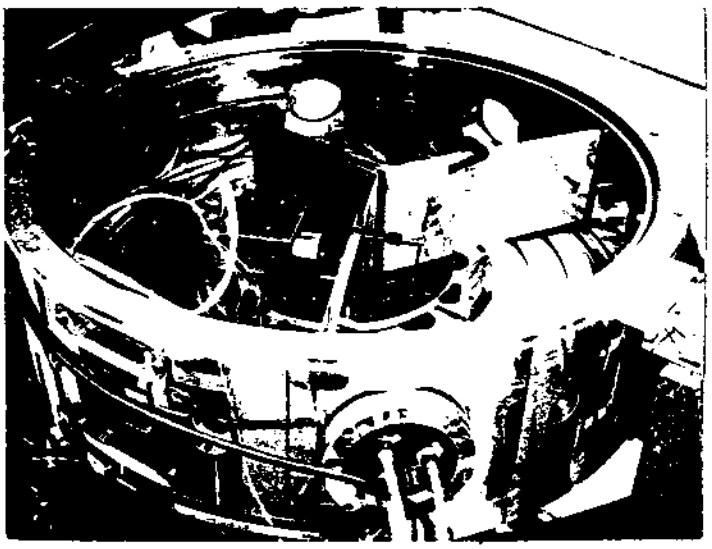

View of scattering chamber showing Telescope mounted on rotating assembly.

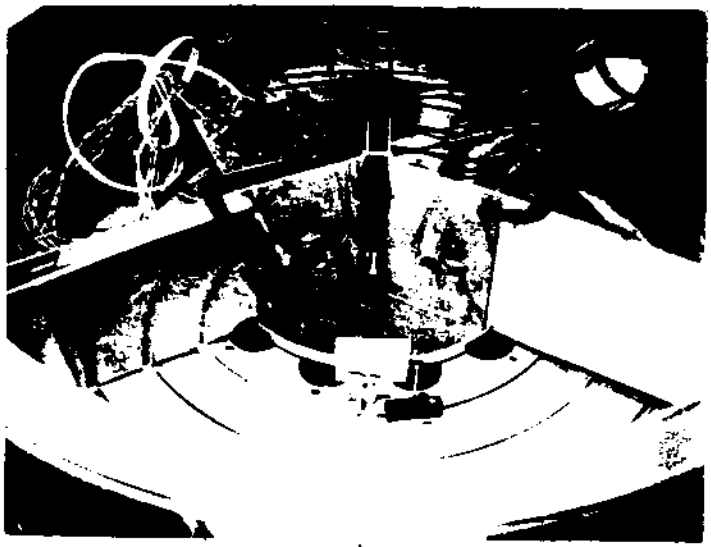

Beam Direction

View from beam direction. Monitor and Telescope view scattering foil thru holes in thick copper plate - monitor is behind hole on right.

Figure 1.10 Telescope on Rotating Platform Mount at the Harvard Cyclotron.

was mounted on a linear scanning platform and used to check the proton beam uniformity across the four inch diameter absorber area of the rotating absorber wheel. These tests showed that for all beam energies used, the lead (Pb) absorber/spreaders (Figure 1.6) provide a beam uniform to about 10% over the monitor detector/DOME separation of Figure 1.6.

The second monitor detector was used without any collimation but had its sensitive area calibrated by the use of alpha sources and collimators in a vacuum chamber. The first monitor detector, collimated as shown in Figure 1.6, had an effective area which was different from the collimator area and varied somewhat with energy. This was the result of the narrow acceptance angle of the collimator (about 10^{o} maximum), the large beam angular spread produced by the Pb absorber/scatters, and the Al/Cu absorbers on the absorber wheel. The second monitor detector responds to the proton fluxes more nearly like the DOME detectors, which have large acceptance angles, and was thus used to provide an absolute calibration for the DOME unit detection areas and geometric factors. By cross-calibrating the first monitor detector to the second monitor detector, all earlier runs made with only the first monitor detector were provided with an absolute calibration.

2. PRIMARY GEOMETRICAL FACTOR DETERMINATION

2.1 Method of Approach

2.1.1 Basic Energy Dependent Geometrical Factor

For a detector such as the DOME in Figure 1.1, the count rate per unit solid angle $C(E, \Omega)$, cps/sr, due to an angular flux of particles of energy E from direction Ω, $F(E,\Omega)$, p/(cm^2 - sr - sec), can be written

$$C(E,\Omega) = dC_o(E,\Omega)/d\Omega = F(E,\Omega)\, A(E,\Omega) \qquad (2.1)$$

where $A(E,\Omega)$, cm^2, is the effective area of the sensor in the direction of Ω, and C_o, cps, is the count rate found by integrating over Ω:

$$C_o(E) = \int F(E,\Omega)\ A(E,\Omega)\ d\Omega \qquad (2.2)$$

For an isotropic angular flux, F can be removed from the integral, and

$$C_o(E) = F(E) \int A(E,\Omega)\ d\Omega \qquad (2.3)$$

$$= F(E)\ \ G(E) \qquad (2.4)$$

where $G(E) = \int A(E,\Omega)\ d\Omega$ cm^2 - sr (2.5)

is the isotropic geometrical factor for energy E. For an analytical determination of G(E), it is convenient to express the count rate per unit solid angle $C(E,\Omega)$ as a function of $F(E,\Omega)$ and the detection system parameters, and then find $A(E,\Omega)$ by use of (2.1):

$$A(E,\Omega) = C(E,\Omega)/F(E,\Omega) \tag{2.6}$$

This result is then placed in (2.5) and integrated over Ω to find G(E).

Experimentally, the particle beam in Figure 1.3 is almost monodirectional, so that the solid angle is quite small. In that case, it is convenient to write $A(E,\Omega)$ from (2.1) as

$$A(E,\Omega) = \frac{dC_o(E,\Omega)}{F(E,\Omega)\,d\Omega} \approx \frac{\Delta C_o(E,\Omega)}{\Delta I(E,\Omega)} \tag{2.7}$$

where, in direction Ω, ΔC_o is the increment of count rate produced by a measured increment of essentially monodirectional angular intensity

$$\Delta I(E,\Omega) = F(E,\Omega)\,\Delta\Omega \qquad p/(cm^2 - sec) \tag{2.8}$$

Thus, in both the analytical and experimental cases, the isotropic geometrical factor is found by use of Eq. (2.5).

For determination of $A(E,\Omega)$, however, (2.7) is better for the experimental determination of G(E), while (2.6) is used for the analytical approach. Furthermore, we note that there are variables upon which the count rate depends that are not shown in (2.6) or (2.7). These are assumed to be contained implicitly and are discussed below.

2.1.2 Experimental Energy Dependent Geometrical Factor

Experimentally, as described in Section 1, the approach is to irradiate the DOME at different angles of incidence with a particle flux of known intensity, having known energy, and measure the counts produced. In that way, the geometrical factor is defined by use of (2.7) and (2.5). The intensity ΔI is just the rate at which particles are incident on a spherical surface, in part/$(cm^2 - sec)$, which is obtained by measurement of the counts C_m recorded in some time t by the monitor detector, (Figure 1.6) whose area is A_m. The intensity is $C_m/(A_m t)$, $(cm^2 - sec)^{-1}$ at the monitor detector, and if the corrected area is used (Section 4.2), then this is the same as the intensity at the DOME detector. Thus, the DOME intensity is taken as

$$\Delta I = C_m/(A_m t) \tag{2.9}$$

During this time t the counts recorded in the DOME are C_d. Hence, by replacing the integral with a summation over the number of values of i used, we obtain

$$G(E) = \frac{A_m t}{t} \sum_i \frac{C_d(\Omega_i)}{C_m(\Omega_i)} \Delta\Omega_i \qquad (2.10)$$

Thus, $C_d(\Omega_i)$ and $C_m(\Omega_i)$ are the values of those quantities recorded while the DOME is oriented at Ω_i (= θ_i, ϕ_i degrees) to the incident particle direction. These can vary with time, of course, but use of the monitor in this way eliminates the temporal effects. Hence, t cancels in (2.10) and the result is

$$G(E) = \sum_i N(\Omega_i) G_i \qquad (2.11)$$

where the number of DOME counts observed per monitor count, while the DOME is oriented at angle Ω_i, is

$$N(\Omega_i) = C_d(\Omega_i)/C_m(\Omega_i) \qquad (2.12)$$

and a geometrical factor associated with the particular measurement at angle Ω_i is

$$G_i = A_m \Delta\Omega_i \qquad (2.13)$$

which, by integration over the polar angles becomes

$$G_i = A_m \Delta\phi_i (\sin\theta_{2i} - \sin\theta_{1i}) \qquad (2.14)$$

Here $\Delta\phi_i$, radians, is the width of the ϕ bin centered on ϕ_i, and the range θ_{1i} to θ_{2i} is centered on θ_i.

The procedure then is to measure $C_m(\Omega_i)$ and $C_d(\Omega_i)$ at a series of values of Ω_i. $N(\Omega_i)$ is calculated from (2.12), and since A_m is known, the G_i are found from (2.14). Then G(E) is calculated from (2.11).

2.1.3 Analytical Energy Dependent Geometrical Factor

The DOME detectors have a broad set of view angles, covering approximately $\pm 30^\circ$ in θ and $\pm 60^\circ$ in ϕ, where θ is the view angle to the detector normal in the plane shown in Figure 1.1, and ϕ is the

angle in the plane of Figure 1.2. This large fan-shaped acceptance cone makes direct calculation of the DOME geometric factors more difficult than for the simpler, smaller angle cylindrical symmetry of the telescope (Ref. 1.9). The high particle energy range of the DOME unit also makes the collimator edge effects more important because of the large particle ranges in even high density materials such as tungsten. The large range in ϕ ($\pm 60^{\circ}$) also means that detector edge effects (particles passing through the edge of a cylinder rather than throught the entire thickness) become important, particularly for the channels P4/E1 in D3 and the channels P6/P7 in D5.

The above factors mean that the experimentally measured G(E) values (Eq. (2.11)) are always to be used for the DOME, with theoretical values only providing some guidance as to the approximate values. A theoretical G value, neglecting the above factors, can be derived by numerically integrating over the (θ, ϕ) angles. For an interval (θ_1, ϕ_1) to (θ_2, ϕ_2), the solid angle increment is

$$\Delta\Omega_{12} = (\phi_2 - \phi_1)(\sin\theta_2 - \sin\theta_1) \tag{2.15}$$

which is simillar to (2.14).

The effective detector area at the angle (θ, ϕ) is

$$A(\theta, \phi) = A_o \cos\theta \cos\phi \tag{2.16}$$

where $A_o = A(0, 0)$ is the total detector sensitive area at normal incidence. Equation (2.16) is an approximation accounting for the effects of the tungsten collimator. As shown at the bottom of Figure 1.5, the two solid state detectors in one DOME module are separated by their diameter, forming a cylinder with a height equal to the diameter. The detectors are 1.5 mm thick, so the gap between them is only 2.6 mm; therefore, for angles up to at least 60°, the area of the uncollimated detector pair is more nearly constant. The tungsten collimator makes (2.16) a better approximation for the DOME units, and from Figure 1.1, at $\phi = 60^{\circ}$ it appears better to reduce (2.16)) by an additional factor of 2 to account for partial shadowing of the front detector by the collimator edges.

The (θ, ϕ) angles were split up into 15° increments, centered on $\theta = 0^{\circ}$, 15°, and 30°, and $\phi = 0^{\circ}$, 15°, 30°, 45°, and 60°. Symmetry was used to split the acceptance cone into four quarters, so only positive (θ, ϕ) were used. The resulting parameters are given in Table 2.1, with $\Delta\Omega_i$ from (2.15), and the A_i/A_o values coming from (2.16). The additional area factor of 0.5 for $\phi = 60^{\circ}$ was justified above. The result sums to give

$$G_{calc} = 1.96\, A_o \tag{2.17}$$

TABLE 2.1

Parameters for Calculating the DOME Geometric Factor

Central θ, ϕ (degrees)	Range in θ, ϕ (degrees)	Number of bins from symmetry	$\Delta\Omega$ for bin (Eq. (2.15)) (sr)	A_i/A_o (Eq. (2.16))	Additional Area Factor*	$\Delta G_i/A_o$ (sr)
0, 0	(-7.5, 7.5), (-7.5, 7.5)	1	0.0683	1.000	1.0	0.0683
0, 15	" , (7.5, 22.5)	2	0.0683	0.969	1.0	0.1320
0, 30	" , (22.5, 37.5)	2	0.0683	0.866	1.0	0.1184
0, 45	" , (37.5, 52.5)	2	0.0683	0.707	1.0	0.0967
0, 60	" , (52.5, 67.5)	2	0.0683	0.500	0.5	0.0342
15, 0	(7.5, 22.5), (-7.5, 7.5)	2	0.0660	0.966	1.0	0.1275
15, 15	" , (7.5, 22.5)	4	0.0660	0.933	1.0	0.2464
15, 30	" , (22.5, 37.5)	4	0.0660	0.837	1.0	0.2209
15, 45	" , (37.5, 52.5)	4	0.0660	0.683	1.0	0.1803
15, 60	" , (52.5, 67.5)	4	0.0660	0.483	0.5	0.0638
30, 0	(22.5, 37.5), (-7.5, 7.5)	2	0.0592	0.866	1.0	0.1025
30, 15	" , (7.5, 22.5)	4	0.0592	0.837	1.0	0.1981
30, 30	" , (22.5, 37.5)	4	0.0592	0.750	1.0	0.1776
30, 45	" , (37.5, 52.5)	4	0.0592	0.612	1.0	0.1450
30, 60	" , (52.5, 67.5)	4	0.0592	0.433	0.5	0.0513
					$\sum = G/A_o =$	1.96

*See text for discussion.

which normalizes G_{calc} to the detector area. The result (2.17) is expected to be accurate to better than 50% for the center energies of a particular bin and may be somewhat too large since all the neglected factors tend to decrease G_{calc}.

2.1.4 Average Geometrical Factor

At times it is adequate not to take into account the detailed energy dependency of the flux within a given energy region, such as in each channel, but to make the approximation that, essentially, the flux is constant within the region.

Here, we will present results for an isotropic differential (in energy) angular flux spectrum f(E), $(cm^2 - sec - sr - MeV)^{-1}$. The number of particles between E and E + dE is then f(E) dE, and the count rate for a specified G(E) is

$$c = \int f(E)\, G(E)\, dE \tag{2.18}$$

If it is assumed that f(E) is essentially constant over the region of interest, defined by "limits" E_{1i} and E_{2i}, then

$$f(E) \approx f(\bar{E})$$

$$\text{where } \bar{E} = (E_{2i} + E_{1i})/2 \tag{2.19}$$

is the average energy characterizing that region, and

$$c(E) \approx \bar{f}(E) \int G(E)\, dE$$

Now the integral can be written

$$\bar{G}(E)\, \Delta E \equiv \int G(E)\, dE$$

$$\text{where } \Delta E = E_{2i} - E_{1i} \tag{2.20}$$

thus defining $\bar{G}(E)$ as

$$\bar{G}(E) = \frac{1}{\Delta E} \int G(E)\, dE \tag{2.21}$$

Hence, c(E) can be expressed as

$$c(E) = \overline{f}(E)\,\overline{G}(E)\,\Delta E \qquad (2.22)$$

within the approximate range ΔE.

Given the count rate and $\overline{G}(E)\,\Delta E$, the average flux in the region is given by:

$$\overline{f}(E) = c(E)/(\overline{G}(E)\,\Delta E) \qquad (2.23)$$

In the case of the primary geometrical factor determination, there is generally only one value of $\overline{G}(E)$ of interest: that averaged over the channel limits and called the "channel average geometrical factor". However, for spurious responses, there may be several energy regions which contribute to a given energy channel; and those are called the "spurious average geometrical factors" for a given energy channel. Effectively, the calculated spurious counts in the channel of interest must be subtracted from observed counts before the average flux in the channel can be defined by use of (2.23).

The quantity $\overline{f}(E)$ determined from (2.23) is then to be interpreted as the approximate number of particles/(cm^2 - sec - sr - MeV) in the region E_{1i} to E_{2i}. It is a relatively crude approximation, which can be improved significantly by straightforward reiteration methods involving assumptions about the dependence of f(E) on E, other than that f(E) is constant within the region. The details of such approaches are beyond the scope of the present effort, however, (See Ref. 2.1 for some examples).

2.2 Results

2.2.1 Experimental Energy Dependent Geometrical Factor

The experimental data are in the form of the number of counts, C_d, recorded in a given energy channel at angles Ω during the time t required for the monitor detector to record a fixed number of counts, usually 10^4 for reasons of statistical accuracy. This allows a determination of $N(\Omega)$, as defined in Eq. (2.12), which is the quantity of interest. From the values of $N(\Omega)$ at the various values of Ω, the energy dependent geometrical factor, G(E), is determined by use of Eq. (2.11).

The particle energies and angles used at the Harvard Cyclotron and the BNL Tandem Van de Graaff for the Engineering Model DOME are given in Tables 1.3 and 1.4. Tables 1.5 and 1.6 list the additional data

acquired with the Protoflight, Flight One, and Flight Two units. The experimental geometric factors were summed over 15° angle increments in (θ, ϕ), with θ going from 0° to 45°, and ϕ from 0° to 60°. The angular ranges, number of symmetry bins, and $\Delta\Omega_i$ values are given in Table 2.2, which is similar to Table 2.1 except for the extension of θ to 45°. The (θ, ϕ) = (45°, 60°) bin is not included since it is generally negligible.

The only complete angle scans were made with the Protoflight DOME, with 25 MeV (D3), 51 MeV (D4), and 94 MeV (D5) (Table 1.5). The angular scan data were reduced to responses relative to $A_o = A(0, 0)$ to allow calculation of the G/A_o ratio directly as in Table 2.1 for the theoretical value. The results for D3(P4/E1), D4(P5), and D5(P6/P7) are given in Table 2.3 and correspond to the approximate central energies of each primary proton bin. The results for P4 + E1 and P6 + P7 are also shown since these correspond more closely to the conditions for the theoretical G/A_o value in (2.17).

The average of the G/A_o value for (P4 + E1), P5, and (P6 + P7) is 1.26, which is about 36% less than the theoretical value in Table 2.1. Comparison of the A_i/A_o values in Table 2.1 with the relative area values of Table 2.3 shows that most of the difference comes from a faster fall at the large θ, ϕ values, which comes from collimator and detector edge effects as discussed briefly in Section 2.1.3.

The engineering model DOME data in Tables 1.3 and 1.4 do not provide all of the angular measurement points listed in Table 2.3 but cover most of the places where significant change occurs. The energy/angle response data for a given DOME channel were interpolated (or extrapolated) in energy and/or angle to provide a full set of angular points for each energy. These data were then used to obtain a numerical G/A_o factor using the $\Delta\Omega_i$ and bin number values from Table 2.2. The resulting G/A_o values are plotted in Figures 2.1, 2.2, and 2.3. The three figures also show the average A_o values for the three flight units (PF, F-1, and F-2), which were found to be nearly equal. By interpolation, the G/A_o values were obtained for all energies where A_o values were measured, and the resulting G values are plotted in Figures 2.4, 2.5, and 2.6. The G values correspond to that from the primary collimator cone and do not include back entering particles through the copper plug (Figures 1.1 and 1.2) (threshold about 80 MeV for protons) and from particles penetrating the tungsten collimator (threshold about 120 MeV). The G factors for these higher energy particles are discussed in Section 3.

In Figures 2.1, 2.2, and 2.3, the G/A_o values are nearly constant over the primary bin widths and peak at the high energy tail where A_o

TABLE 2.2

Angular Bins Used to Obtain Experimental DOME Geometric Factors

Central θ, ϕ (degrees)	Range in θ, ϕ (degrees)	Number of bins from symmetry	$\Delta\Omega_i$ (sr)
0, 0	(-7.5, 7.5), (-7.5, 7.5)	1	0.0683
0, 15	" , (7.5, 22.5)	2	0.0683
0, 30	" , (22.5, 37.5)	2	0.0683
0, 45	" , (37.5, 52.5)	2	0.0683
0, 60	" , (52.5, 67.5)	2	0.0683
15, 0	(7.5, 22.5), (-7.5, 7.5)	2	0.0660
15, 15	" , (7.5, 22.5)	4	0.0660
15, 30	" , (22.5, 37.5)	4	0.0660
15, 45	" , (37.5, 52.5)	4	0.0660
15, 60	" , (52.5, 67.5)	4	0.0660
30, 0	(22.5, 37.5), (-7.5, 7.5)	2	0.0592
30, 15	" , (7.5, 22.5)	4	0.0592
30, 30	" , (22.5, 37.5)	4	0.0592
30, 45	" , (37.5, 52.5)	4	0.0592
30, 60	" , (52.5, 67.5)	4	0.0592
45, 0	(37.5, 52.5), (-7.5, 7.5)	2	0.0483
45, 15	" , (7.5, 22.5)	4	0.0483
45, 30	" , (22.5, 37.5)	4	0.0483
45, 45	" , (37.5, 52.5)	4	0.0483

TABLE 2.3

Measured Angular Responses and G/A_o Values for the Protoflight DOME at the Approximate Bin Center Energies for Protons

θ, ϕ (degrees)	D3 at 25 MeV			D4 at 51 MeV	D5 at 94 MeV		
	Rel (P4)	Rel (E1)	Rel (P4+E1)	Rel (P5)	Rel (P6)	Rel (P7)	Rel (P6+P7)
0, 0	1.000	1.000	1.000	1.000	1.000	1.000	1.000
0, 15	0.878	1.115	0.950	0.884	0.894	1.384	0.944
0, 30	0.591	1.177	0.767	0.697	0.656	1.372	0.727
0, 45	0.409	0.834	0.537	0.442	0.454	0.622	0.471
0, 60	0.173	0.261	0.200	0.162	0.218	0.297	0.226
15, 0	0.866	0.912	0.881	0.852	0.745	1.128	0.766
15, 15	0.789	1.019	0.859	0.765	0.694	0.912	0.715
15, 30	0.569	1.057	0.716	0.608	0.570	0.810	0.594
15, 45	0.393	0.730	0.495	0.389	0.346	0.408	0.352
15, 60	0.127	0.227	0.157	0.179	0.139	0.245	0.150
30, 0	0.317	0.767	0.451	0.503	0.349	0.534	0.367
30, 15	0.252	0.566	0.346	0.445	0.264	0.461	0.284
30, 30	0.155	0.496	0.257	0.317	0.200	0.239	0.204
30, 45	0.057	0.160	0.088	0.166	0.089	0.166	0.097
30, 60	0.006	0.020	0.011	0.032	0.024	0.065	0.028
45, 0	0.002	0.010	0.004	0.021	0.010	0.026	0.012
45, 15	0.000	0.017	0.005	0.010	0.013	0.025	0.014
45, 30	0.000	0.000	0.000	0.007	0.004	0.000	0.003
45, 45	--	--	--	0.004	--	--	--
Resulting G/A_o *	1.11	1.84	1.33	1.29	1.11	1.64	1.16

*G/A_o calculated using the $\Delta\Omega_i$ and bin numbers from Table 2.2.

Figure 2.1 D3 DOME - Measured G/A_o and A_o Values

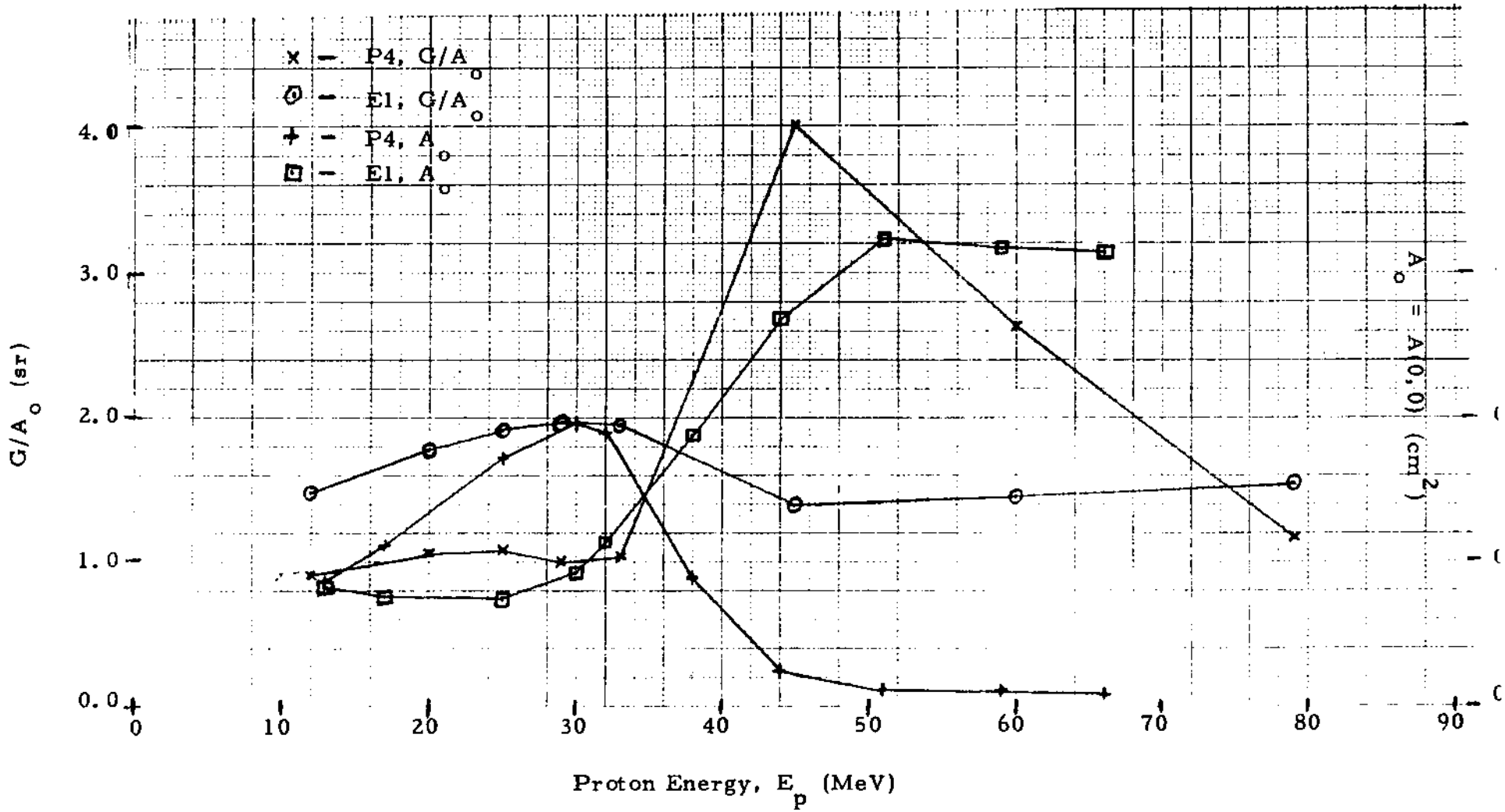

Figure 2.2 D4 DOME - Measured G/A_o and A_o Values

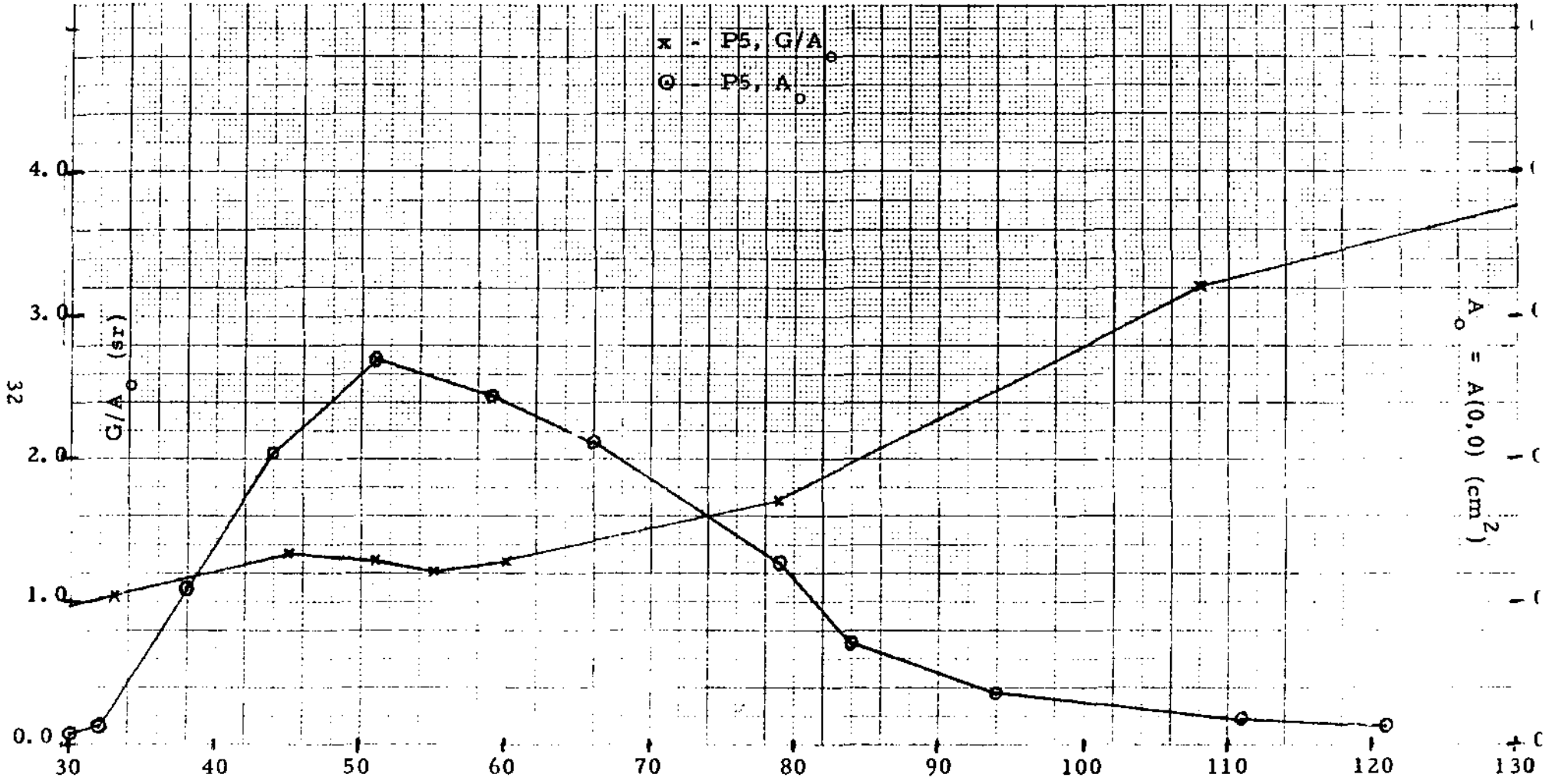

Figure 2.3 D5 DOME - Measured G/A_o and A_o Values

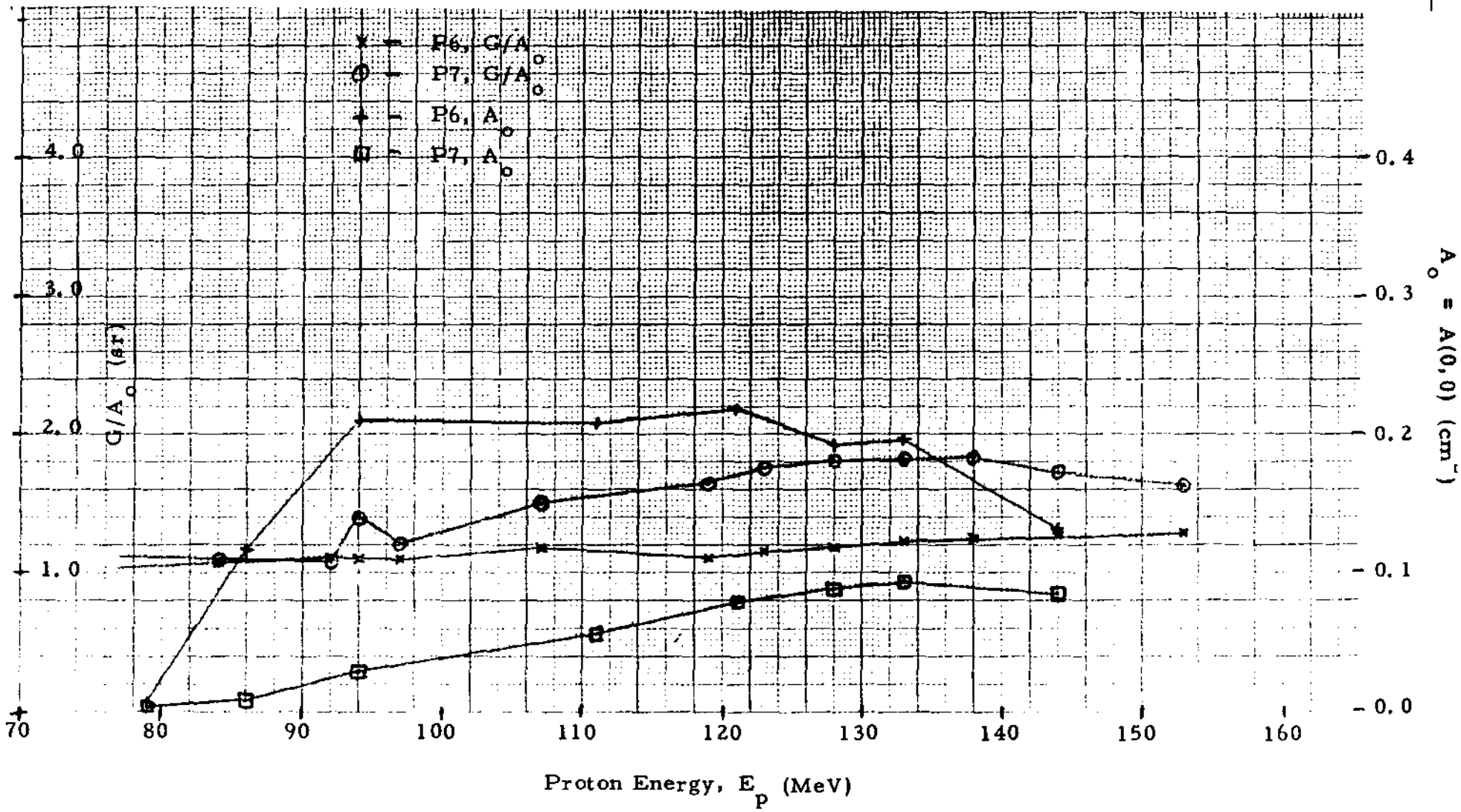

Figure 2.4 D3 DOME - Measured G(E) Values

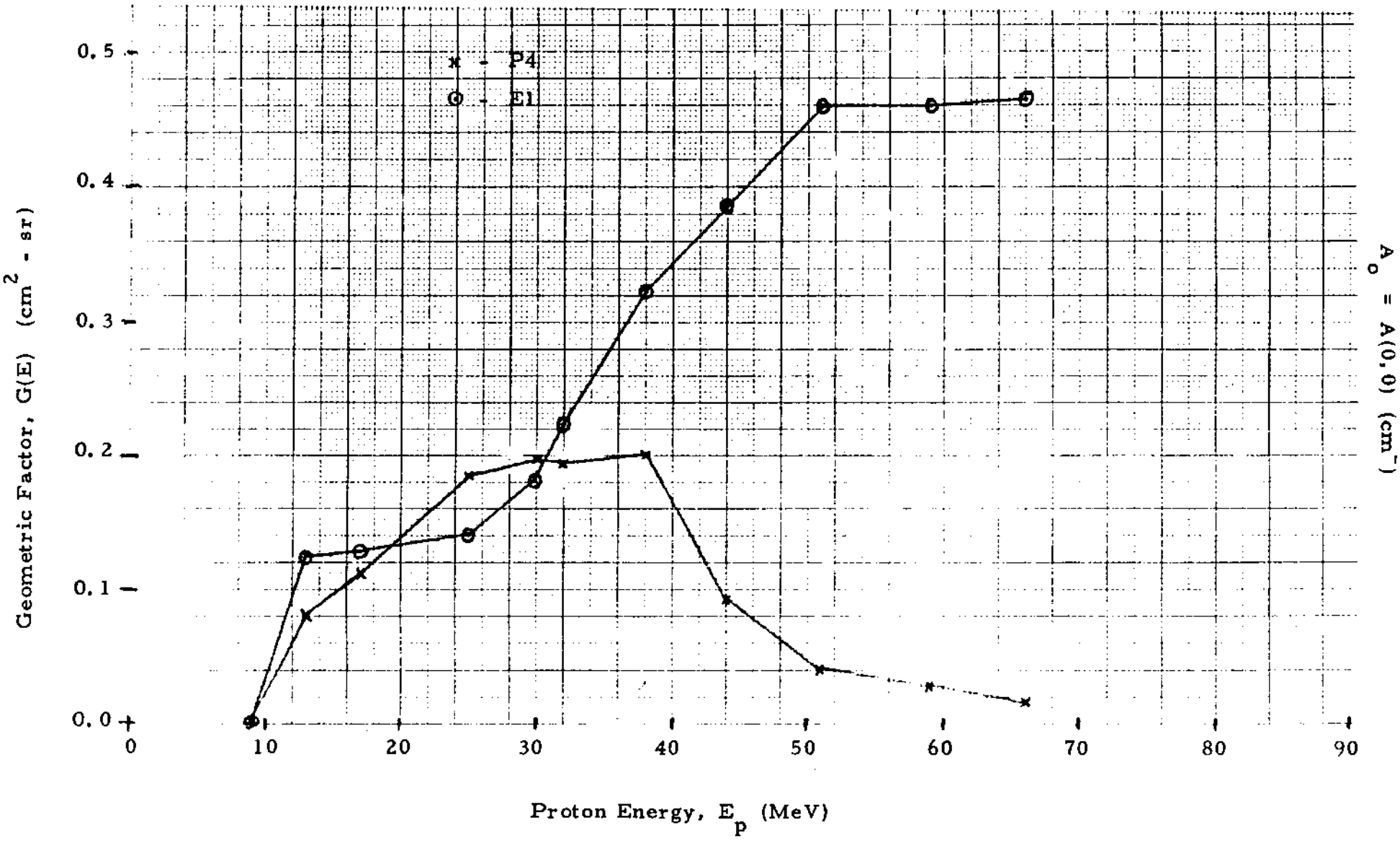

Figure 2.5 D4 DOME - Measured G(E) Values

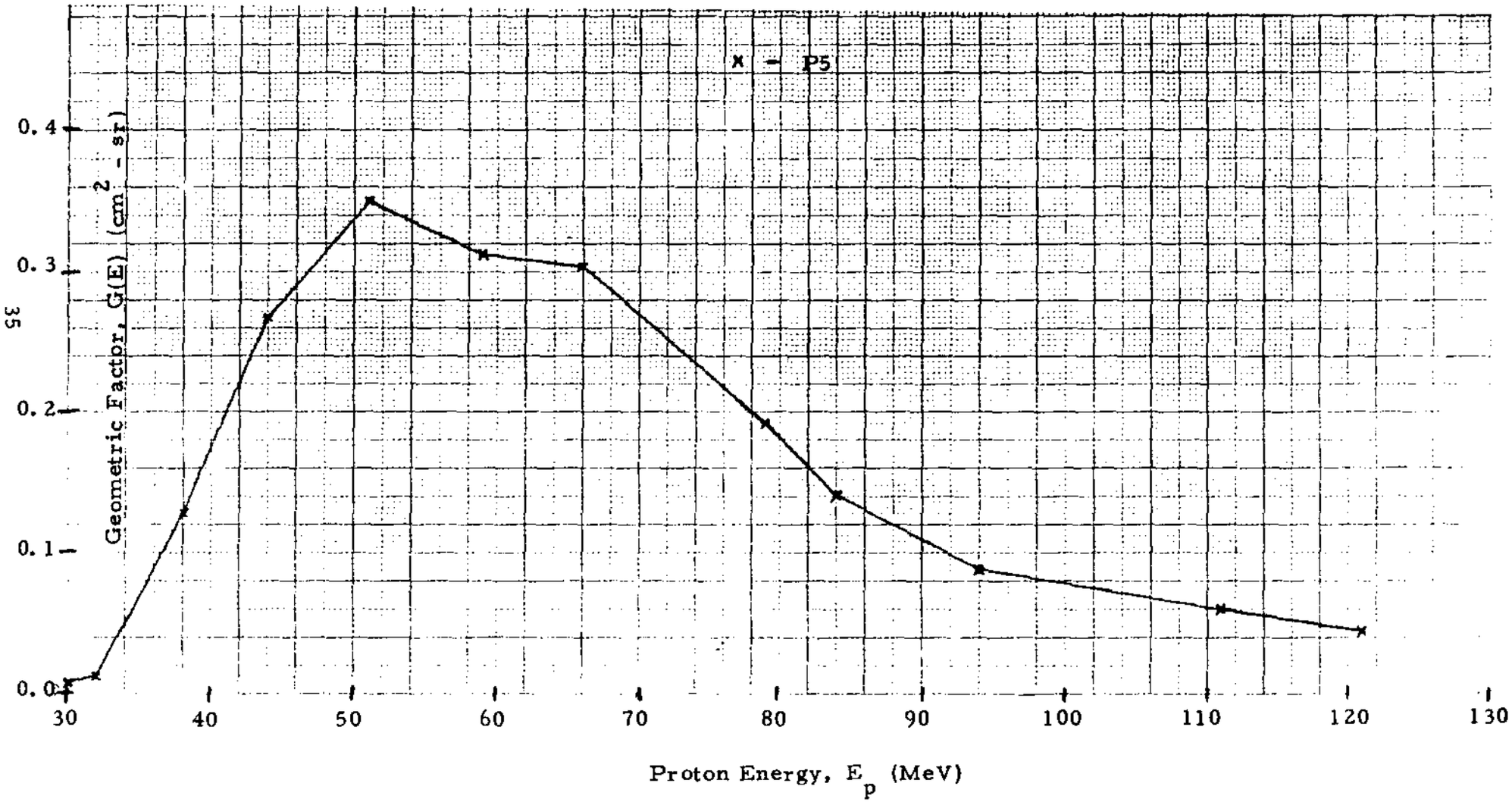

Figure 2.6 D5 DOME - Measured G(E) Values

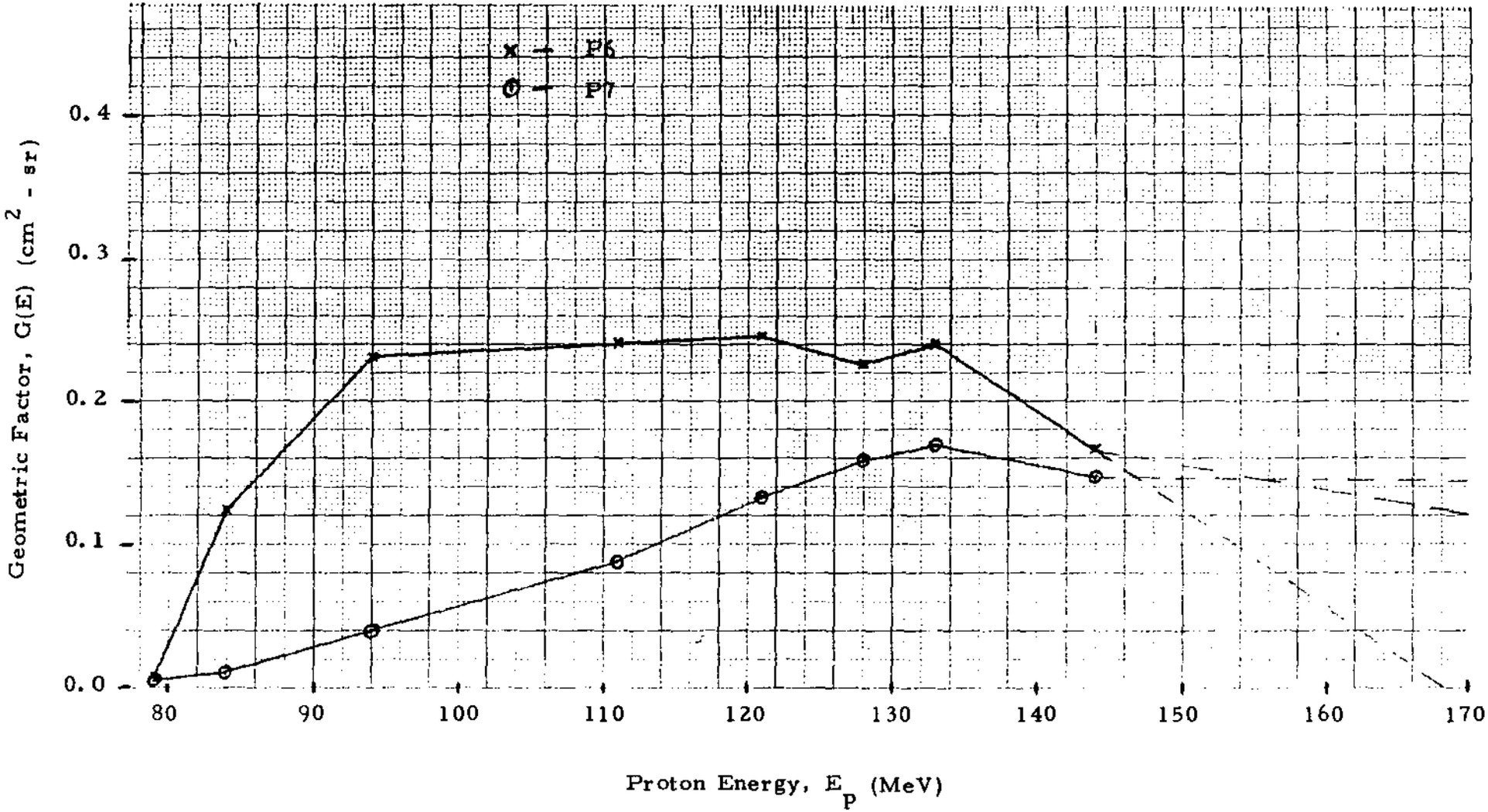

has decreased. The latter result comes from the high energy bin extension for non-normal entry particles. The central bin averages of G/A are 1.55 for D3 (P4 + E1), 1.29 for D4 (P5), and 1.35 for D5 (P6 + P7), giving an overall average of 1.40. This is slightly higher than the average from Table 2.3 and is about 30% less than the theoretical value of Eq. (2.17).

The G(E) values plotted in Figures 2.4 and 2.5 are complete for P4 and P5 and should be reasonably constant for E1 up to a few hundred MeV for protons. The P6 and P7 results in Figure 2.6 show only the rise in P7 and the start of the high energy fall-off for P6. Possible extensions are indicated by the dotted lines, with the nearly flat responses being the more likely. Above 140 MeV, the response is more nearly isotropic and is discussed more fully in Section 3.

The ϕ angle distribution, $G(\phi)$, is shown in Table 2.4 for the data of Table 2.3. These are typical angular sensitivities in the plane of Figure 1.2, above (and below) the satellite equatorial plane, for particles near the central bin energies. For higher energies near the upper bin edges, the distribution spreads out to larger angles, peaking near $\pm 15^{\circ}$ to $\pm 30^{\circ}$. The summed response from the $\pm 60^{\circ}$ angles is about 30% of the response at 0°, so the DOME provides a good angular measure to $\pm 60^{\circ}$ from the spin plane.

2.2.2 Channel Average Geometrical Factor

The G(E) plots in Figures 2.4, 2.5, and 2.6 give the geometrical factors for the primary bins for all three flight unit DOME sensors. The G(E) curves can be used to obtain complete channel average geometrical factors for P4 and P5 and reasonable extrapolated values for E1, P6, and P7. Since the alpha particle channels should behave similar to the proton channels when compared on an energy/nucleon basis (see Figures 1.3, 1.4, and 1.5), the calculated alpha particle channels of Table 1.2 can be corrected by the proton data. This is done by taking the corrected alpha bin limit as equal to the calculated alpha bin limit multiplied by the ratio of measured/calculated bin limits for the proton bin of the same DOME.

The channel average geometrical factors were calculated using the procedures of Section 2.1.4. The energy limits, E_{1i} and E_{2i} were chosen as the energies where G(E) falls to about half of the central bin average. The results are given in Table 2.5. For P4 and P5, the values are quite accurate since the full energy range was measured (Figures 2.4 and 2.5). The corresponding corrected alpha particle channels, A4 and A5, should also be reasonably accurate. The P6 and P7 values for E_{1i} should also be accurate, but the E_{2i} values are based primarily on the theoretical values. The $\overline{G}$ values for P6 and P7 are based on the maxima of Figure 2.6. The

TABLE 2.4

$G(\phi) / A_o$ Measured Angular Responses for the Proto-Flight Dome

ϕ (degree)	D3 at 25 MeV			D4 at 51MeV	D5 at 94 MeV		
	P4	E1	P4+E1	P5	P6	P7	P6+P7
0	0.220	0.280	0.238	0.242	0.209	0.283	0.214
±15	0.194	0.279	0.220	0.215	0.185	0.272	0.194
±30	0.134	0.279	0.177	0.166	0.144	0.229	0.153
±45	0.087	0.172	0.112	0.102	0.087	0.116	0.090
±60	0.029	0.050	0.036	0.038	0.036	0.060	0.039
Sum =	1.11	1.84	1.33	1.28	1.11	1.64	1.17

Note: based on data of Table 2.3. Minor differences (±0.01) in the Sum are from round-offs at different stages of the calculation.

TABLE 2.5

Experimental/Corrected Channel Average Geometrical Factors

Channel	E_{1i} (MeV)	E_{2i} (MeV)	ΔE (MeV)	$\bar{E}$ (MeV)	$\bar{G}$ (cm^2-sr)
P4	15	44	29	29.5	0.21
P5	39	82	43	60.5	0.36
P6	84	(200)	116	142	0.28
P7	110	(500)	390	305	0.16
A4*	60	180	120	120	0.21
A5*	160	260	100	210	0.36
A6*	330	(500)	170	415	0.28
E1†	32	(≈500)	(468)	(266)	0.46

*Alpha particle bins are corrected values based on the proton measurements.

†This is for the E1 response to protons. Note that the response has a two-step rise (see Fig. 2.4).

Note: Values in parentheses are based primarily on the theoretical estimates.

A6 values are derived from the P6 values. For E1, the E_{1i} value is from Figure 2.4, but note that the rise consists of a double step while only one-half height value is listed. The E_{2i} value for E1 is the approximate theoretical value.

The calculated $\bar{G}$ for a DOME channel based on Table 2.1 and a 0.25 cm^2 detector set is 0.49 cm^2-sr. The value for E1 (0.46 cm^2-sr) is close to this as is the P5 value (0.36 cm^2-sr). Because of energy loss straggling by the protons and detector edge effects (corners) at non-normal incidence, the P4/E1 and P6/P7 channels tend to merge. For P4, the E1 channel is just as sensitive (Figure 2.4), and this explains the low $\bar{G}$ for P4 (0.21 cm^2-sr, about half the theorectical value). Similarly, P6 and P7 tend to merge (Figure 2.6), and so both have a $\bar{G}$ lower than the theoretical value.

The primary bin geometrical factors of Table 2.5 are reasonably accurate and should be used for most data analysis. Note that all bins have additional geometrical factors above 80 MeV and 120 MeV protons from shielding penetration. These are discussed in Section 3.

2.3 Electron Channel Geometrical Factor

The calculated response of D3 to electrons in channel E1 is shown in Figure 1.3, where the electron energy losses in Al (Ref. 1.4) and Si (Ref. 1.5) have been used. The penetration energy of electrons for the D3 Al shield is about 0.33 MeV, while for the D4 shield, it is 2.6 MeV and for the D5 shield 15 MeV. From Figure 1.3, a threshold of 1.77 MeV of energy loss would give an effective threshold of 2 MeV for electrons in E1 for total energy loss in the Si detectors. The theoretical G would be 0.49 cm^2-sr corrected to about 0.34 cm^2-sr on the basis of the proton scans.

Electrons undergo significant scattering so that the actual energy loss is spread from the total loss curve of Figure 1.3 down to zero energy loss. The detailed energy loss spectra for monoenergetic electrons in silicon detectors has been calculated and measured with extensive results being presented in Ref. 2.2. The transmission of electrons through foils has also been discussed extensively in Ref. 2.3. The data in these two references form the basis for theoretical calculations of the electron detection efficiency of the E1 channel in the D3 DOME.

The theoretical detection efficiency of the E1 channel with a 1.77 MeV threshold depends on two factors: the penetration of electron through the D3 shield; and the deposition of energy in the silicon detectors. Since the D3 DOME shield is 0.125 g/cm^2 of aluminum, it is the range thickness for 0.33 MeV electrons, and minimum ionizing electrons (the range of

about 0.5 to 5 MeV) only lose about 0.19 MeV in penetrating the shield. The data and calculations in Ref. 2.3 show that for electrons of energy $\geq$ 2 MeV the transmission fraction for the D3 shield is nearly 100%, so the shield slightly shifts the average electron energy but does not affect the intensity.

The data and calculations in Ref. 2.2 can be used to calculate the detection efficiency of a silicon detector for several electron energy/detector thickness combinations and for any detector threshold between 0 MeV and the incident electron energy. This involves integration over several spectral curves presented in Ref. 2.2 but yields a table of efficiencies for a number of values of E_{th}/E_e and z/r_o, where E_{th} is the detector threshold (MeV), E_e is the incident electron energy (MeV), z is the detector thickness (g/cm^2), and r_o is the range of the electrons of energy E_e (in g/cm^2). Using this table to interpolate for E_{th} = 1.77 MeV and z = 0.699 g/cm^2 (3000 μm of silicon), the resulting detection efficiencies for 2 to 10 MeV electrons are given in Table 2.6. These theoretical detection efficiencies are likely to be too high for two reasons. First, the theoretical values are for a detector with a large horizontal extent compared to the electron scattering paths, so that there are no edge losses. This is clearly not the case for E1 where the full detector area is irradiated by electrons. And second, the calculations are for a single detector slab, whereas the D3 module contains two 1500 μm detectors separated by about 2.6 mm (2600 μm) (exit face to entrance face). The theoretical detection efficiencies of Table 2.6 show an approximately flat efficiency above 2 MeV, with 2 MeV being a sharp threshold. The actual threshold is not likely to be too sharp but should be at about 2 MeV, and the efficiency should be reasonably constant at higher energies.

The response of the Protoflight DOME E1 channel to Sr-Y-90 (2.27 MeV end point) and to Ru-Rh-106 (3.54 MeV end point) beta sources was measured to provide an experimental correction to the theoretical electron detection efficiencies in Table 2.6. Both beta sources have been calibrated so that the forward beta intensity can be readily calculated. The beta spectra shapes for the two sources are taken from Ref. 2.4. The sources were 45 cm from the D3 DOME and were collimated to reduce air-electron scattering effects. The net electron energy loss in the air and the D3 shield is about 0.25 MeV; therefore, the measured count rates for a given threshold E_{th} (MeV) were compared with the calculated source flux above E_{th} + 0.25 (MeV). The results are shown in Table 2.7.

The beta source results for Sr-Y-90 and Ru-Rh-106 are in good agreement and show that for a threshold of 1.75 MeV the detector efficiency is only about 10%. This is about a factor of three lower than the calculated efficiency in Table 2.6 but is not unreasonable considering the differences between the theoretical conditions and the actual D3 detector

TABLE 2.6

Theoretical Detection Efficiencies of the E1 Channel for Electrons

Incident Electron Energy, E_o (MeV)	Calculated Detection Efficiency for E_{th} = 1.77 MeV
2	0.31
3	0.25
5	0.30
7	0.31
10	0.27

TABLE 2.7

Measured Beta Source Responses of the E1 Channel

Detector threshold energy, E_{th} (MeV)	Source Spectrum threshold (MeV)	Sr-Y-90 Results			Ru-Rh-106 Results		
		Calculated Counts (1 sec)	Measured Counts (1 sec)	(Measured / Calculated)	Calculated Counts (1 sec)	Measured Counts (1 sec)	(Measured / Calculated)
0.5	0.75	2220	1955	0.88	658	586	0.89
1.0	1.25	1080	580	0.54	473	237	0.50
1.5	1.75	228	42.3	0.186	287	53.0	0.185
1.75	2.00	51.4	3.55	0.069	183	20.0	0.109
2.0	2.25	0.0	0.47	--	129	6.52	0.051

The Sr-Y-90 results for E_{th} = 1.75 and 2.00 MeV are questionable because of the closeness to the beta spectrum end-point energy, so the efficiencies at these thresholds are better given by the Ru-Rh-106 results. The net conclusion is that the E1/D3 channel has a threshold of 2 MeV (half of peak detection efficiency) and a detection efficiency of 0.10. With the 0.34 cm^2-sr geometric factor for unit detection efficiency, the E1 channel has a geometric factor for > 2 MeV electrons of 0.034 cm^2-sr.

3. SPURIOUS GEOMETRICAL FACTOR DETERMINATION

3.1 Method of Approach

The DOME detectors are well shielded from protons below about 80 - 115 MeV for all directions outside the primary acceptance cone discussed in Section 2. Above 80 MeV, some protons can penetrate the 8 g/cm^2 copper plug behind the detectors, and above 115 MeV, some can penetrate the tungsten shield of about 20 g/cm^2. For these high energy protons, the detectors have a nearby omnidirectional response with a geometrical factor near 2.5 cm^2-sr. Since the primary geometrical factors are near to 0.30 cm^2-sr, the spurious (shielding-penetrating particle) geometrical factor will dominate at high energies. This is especially true for P6 and P7 (and A6), the highest energy channels.

The spurious geometrical factors were calculated using detailed response calculations for several particle arrival directions, allowing for variations in shielding and in detector thickness. The calculated energy-dependent geometrical factors were then compared to experimental values; and final experimentally corrected spurious geometrical factors derived. The method is discussed in more detail in the following sections, which also give the final corrected spurious geometrical factors.

3.2 Results

3.2.1 Analytical

The basic DOME module construction is shown in Figure 1.2, where the detector volume, tungsten shielding, and rear copper plug shielding are all illustrated. The spurious geometrical factors arise from particles penetrating the tungsten and copper plug shielding. Most of these particles have also penetrated various amounts of spacecraft structure so that the actual shielding is somewhat variable. The DOME structure also introduces some variability into the shielding thickness for different directions; therefore, the response calculation is not as straightforward as for the primary geometrical factors in Section 2.

The basic components for the spurious geometrical factors are given in Table 3.1, which provides the solid angle, area, shielding, and detector thickness for a decomposition into five angular bins. The solid angle is just 2π ($\cos\theta_1 - \cos\theta_2$), while the detector area shows only small changes with angle. The latter is because two 0.15 cm thick, 0.56 cm diameter stacked discs have 0.25 cm^2 area for normal incidence and 0.17 cm^2 area edge on ($\theta = 90^\circ$). The copper plug is used for shielding from 135° to 180° and tungsten for the remaining angle ranges. The

TABLE 3.1

Basic Components For Calculating the Spurious Geometrical Factors

θ angle range (degrees)	ΔΩ solid angle (sr)	$\overline{A}$ area (cm^2)	Shielding description			Si detector thicknesses in microns	
			Material	Thicknesses (g/cm^2) Average	Range	Average	Range *
165-180	0.214	0.25	Cu	11	8-14	3000	1750-3000
135-165	1.63	0.25	Cu	11	8-14	3000	1750-3000
105-135	2.82	0.20	W	20	18-25	3000	3000-4250
75-105	3.25	0.17	W	20	18-25	4250	3000-4250
45-75	2.82	0.20	W	20	18-25	3000	3000-4250

*Ranges are approximate. In most cases the minimum is 0μ for particles just striking the detector edge.

range in shielding thicknesses are estimates for the effective thickness range. In most cases, the actual range is somewhat larger, in particular extending to 0 μ for edge penetrating particles. The final thicknesses have been rounded to 3000 ± 1250 microns to provide a reduced set for calculations, giving each angular range only two detector thicknesses.

The several absorber thickness/detector thickness combinations in Table 3.1 were used with the procedure described in Section 1 to calculate the proton energies corresponding to the various detector energy thresholds. From this a table of proton energy detection ranges was generated for each particle channel (E1 to P7) and each angular range in Table 3.1. The two detector thicknesses for each angular range were then combined with a relative weight based on the estimated fractional areas effective for each thickness (the 165-180 degree bin had given the 3000/1750 thicknesses a relative weight of 7/1 since at near normal incidence few particles can pass through a detector edge). The resulting detection ranges were smeared out over the energy range

given by the absorber thickness range, broken into smaller energy ranges, and then summed over angle. The resulting calculated spurious geometrical factors are given in Table 3. 2.

3. 2. 2 Experimental

The spurious geometrical factors were measured for a number of proton energies by irradiations at $\theta = 90^{\circ}$, 120°, 150°, and 180° (rear irradiations - see Table 1. 5). Using these data with the $\Delta\Omega$ values of Table 3. 1, and assuming $\theta = 60^{\circ}$ is the same as $\theta = 120^{\circ}$, the resulting measured geometrical factors are given in Table 3. 3, along with the calculated/measured ratios. The E1/P4 results at 79 MeV are right at the threshold and so are quite sensitive to beam energy spread; thus, they are not compared with a theoretical value. The P6 results at 119 MeV have calculated much higher than measured, but this is just past the large jump in the theoretical G at 110 MeV and so is excluded from the second average ratio value. The two low energy P7 ratios are quite low because of P7 sensitivity to lower energy protons. This factor also shows up in the primary geometrical factor for P7 as shown in Figure 2. 6. The second average ratio for P7 excludes the two low energy values.

The average ratios in Table 3. 2 are used to provide a corrected estimate for the spurious G(E) values. These are then used to correct the calculated values in Table 3. 2 and to provide the best estimate values for the spurious G(E) as listed in Table 3. 4. The correction divisors have been rounded off, and the P4 value has been reduced to 2. 0 to avoid excessive weighting from the 94 MeV value. The resulting G(E) values are estimated to be accurate to $\pm 50\%$ on the average but may have larger errors at isolated energies, especially at the breakpoint energies where G(E) changes significantly. The low energy end has an additional uncertainty introduced by the variable and largely unknown shielding of the DOME by the spacecraft structure and other instruments. The lowest energy range for P7 has been increased to be more in accord with the measurements.

The spurious geometrical factors for the alpha particle channels have been calculated from the proton results. The alpha particle/proton energy ranges for the direct bins (Section 2) have been used to normalize the proton energy ranges in Table 3. 4 to obtain the G(E) for A4 from P4, A5 from P5, and A6 from P6. The lowest energies are four times the lowest proton energies; the highest energies are four times (for A4/P4), three times (for A5/P5), and two times (for A6/P6) the highest proton energy with the other energies being linear interpolations.

TABLE 3.2

Uncorrected, Calculated Spurious Geometrical Factors

Particle Channel	Proton Energy Range (MeV)	Calculated Geometrical Factor, G_{calc} (cm^2-sr)
E1	80-90	0.014
	90-110	0.42
	110-125	0.48
	125-300	2.03
	300-800	0.56
P4	80-115	0.076
	115-150	0.49
P5	80-110	0.18
	110-150	1.15
	150-190	0.42
P6	80-110	0.29
	110-130	1.69
	130-200	1.61
	200-300	0.52
P7	80-110	0.0031
	110-170	0.15
	170-250	1.48
	250-500	1.90
	500-900	0.56

TABLE 3.3

Measured Spurious Geometrical Factors and Ratios of Calculated to Measured

Particle Channel	Proton Energy (MeV)	Measured Geometrical Factor (cm^2-sr)	$\left(\frac{\text{Calculated}}{\text{Measured}}\right)$
E1	79	0.062	-
	94	0.098	4.27
	108	0.170	2.46
	144	0.672	3.02
			Average = 3.25
P4	79	0.009	-
	94	0.014	5.42
	108	0.072	1.05
	144	0.345	1.42
			Average = 2.63
P5	92	0.084	2.15
	96	0.133	1.36
	106	0.076	2.38
	144	0.678	1.69
			Average = 1.90
P6	92	0.110	2.65
	106	0.209	1.39
	119	0.239	7.05
	138	0.639	2.51
	153	0.654	2.46
			Average = 3.21/2.25*
P7	92	0.014	0.22
	106	0.040	0.08
	119	0.116	1.28
	138	0.190	0.78
	153	0.302	0.49
			Average = 0.57/0.85†

*This average excludes the 7.05 value.

†This average is only for the last three (3) values.

TABLE 3.4

Corrected Spurious Geometrical Factors for Protons

Particle Channel	Proton Energy Range (MeV)	Corrected Geometrical Factor (cm^2-sr)	Correction Divisor Used
E1	80-90	0.005	3.0
	90-110	0.14	3.0
	110-125	0.16	3.0
	125-300	0.68	3.0
	300-800	0.19	3.0
P4	80-115	0.038	2.0
	115-150	0.25	2.0
P5	80-110	0.091	2.0
	110-150	0.57	2.0
	150-190	0.21	2.0
P6	80-110	0.15	2.0
	110-130	0.84	2.0
	130-200	0.80	2.0
	200-300	0.26	2.0
P7	80-110	0.03	0.10
	110-170	0.15	1.0
	170-250	1.5	1.0
	250-500	1.9	1.0
	500-900	0.56	1.0

The corrected spurious G(E) values in Tables 3.4 and 3.5 are for particles which enter the DOME through the shielding. These are in addition to the direct geometrical factors given in Section 2, and the two must be added to give the total DOME response to high energy particles.

The alpha particle channels also have a spurious response to high energy protons caused by nuclear interactions in the silicon and/or shielding. The results of several measurements at various energies are summarized in Table 3.6. The measurements are generally based on only a few counts each, so the results are near the limits of the measurements. Since the lower energy proton beams were generated by absorbers (lead, copper, aluminum, polyethylene), it is also possible that some of the measured response is actually from contaminants in the proton beam; and therefore, the results in Table 3.6 should be taken as possibly only upper limits. The G(E) values for 150 MeV protons increase from A4 to A5 to A6, while the corresponding thresholds (L8, L10, L13 = 40, 30, 28 MeV) decrease and thus behave as would be expected. The response of A5 below 80 MeV is at the limit of detection and may well be due to proton beam contamination.

4. SUMMARY AND CONCLUSIONS

4.1 Summary

The new design DOME detector assemblies for the GOES D, E and F satellites were calibrated with proton beams to provide experimental energy dependent geometrical factors. Most of the data were taken at the Harvard Cyclotron, with some additional low energy data being taken at the Brookhaven National Laboratory Van de Graaff Accelerator. Data for 12 to 153 MeV protons were acquired. The data were integrated over angle to obtain the primary geometrical factors in Section 2. The spurious geometrical factors for high energy protons penetrating the shielding were treated in Section 3.

The measured and calculated primary geometrical factors agree to about 30%, which is well within the uncertainties of the calculation. The general energy dependence of the G(E) factors is as expected. The spurious geometrical factors for penetrating protons have the measured values as about half of the calculated values, but this is also well within the uncertainty in the calculations due to the complexity of including the variations of shielding and detector thickness with angle. The response of the E1 channel to electrons (beta-particles) was measured to be about 10% efficiency for electrons above 2 MeV. This is about 1/3 the theoretical value for "large area" detectors with no edge losses and is quite

TABLE 3.5

Corrected Spurious Geometrical Factors for Alpha Particles

Particle Channel	Alpha Particle Energy Range (MeV)	Corrected Geometrical Factor (cm^2-sr)
A4	320-460	0.038
	460-600	0.25
A5	320-390	0.091
	390-480	0.57
	480-570	0.21
A6	320-360	0.15
	360-385	0.84
	385-470	0.80
	470-600	0.26

TABLE 3.6

Spurious Geometrical Factors of Alpha Particle Channels for High Energy Protons

Alpha Particle Channel	Proton Energy (MeV)	Geometrical Factor (cm^2-sr)
A4	150	$1x10^{-3}$
	100	$5x10^{-4}$
	<80	$<1x10^{-4}$
A5	150	$5x10^{-3}$
	100	$1x10^{-3}$
	80	$3x10^{-4}$
	<50	$<1x10^{-4}$
A6	150	$8x10^{-3}$
	110	$1x10^{-3}$
	90	$5x10^{-4}$
	<80	$<5x10^{-4}$

reasonable for DOME detector geometry where the edge losses for electrons are expected to be large.

The primary geometrical factors for protons are given in Figures 2.4, 2.5, and 2.6, with the channel average results for protons and alpha particles being given in Table 2.5. The spurious geometrical factors are given in Table 3.4 for protons and Table 3.5 for alpha particles. The E1 channel electron response is given in Section 2.3.

4.2 Conclusions and Comparison with Previous GOES DOME

Proton calibration data for the SMS-A, B, C DOME units are presented in Ref. 1.10, with a copy of the C DOME data being reproduced in Figure 4.1. Although not explicitly stated in Ref. 1.10, the data in Figure 4.1 appear to be for near normal incidence on the DOME and are thus best compared to the A(0, 0) data in Figures 2.1, 2.2, and 2.3. The maximum counts in Figure 4.1 correspond to slightly less than the 9 mm^2 area of one face of the cubical detectors used in these early model DOMEs.

A more complete angular calibration of the GOES B, C DOMEs is described in Ref. 1.11, with a copy of the summary figure being shown in Figure 4.2. The data in Figure 4.2 are effective DOME detector area for an isotropic flux of 1 proton/cm^2, corresponding to a directional flux of $1/4\pi$ proton/(cm^2 - sr). The maximum average detector area is about 0.26 cm^2 for P6 and 0.03 cm^2 for P7, giving a sum of 0.29 cm^2 at 120 MeV. The DOME units described in Ref. 1.11 used 50 mm^2, 3 mm thick Si(Li) detectors, which have a side view area of 24 mm^2 and an average area of about 37 mm^2 (0.37 cm^2) in reasonable agreement with the maximum effective areas in Figure 4.2.

The P4 and E1 curves in Figure 4.2 appear to be interchanged. Comparison with the 40 - 70 MeV data in Figure 4.1 shows this most clearly. Since P4 is nominally for 15 - 40 MeV protons, the P4/E1 data of Figure 4.1 are more in accord with expectations, and so Figure 4.2 most likely should have P4 and E1 labels interchanged.

The GOES D, E and F DOME data for the primary geometrical factors in Figures 2.4, 2.5, and 2.6 have been combined with the spurious geometrical factors in Table 3.4 to give the total geometrical factors plotted in Figure 4.3. The general shapes of the responses are similar to those of Figures 4.1 and 4.2 with the P4/E1 interchange in Figure 4.2. The major difference is that the increase at about 80 MeV in Figures 4.1 and 4.2, from protons penetrating the back shielding plate, takes place at 80 - 90 MeV (penetration of the copper plug behind the detectors - see Figure 1.2) and at 110 - 120 MeV

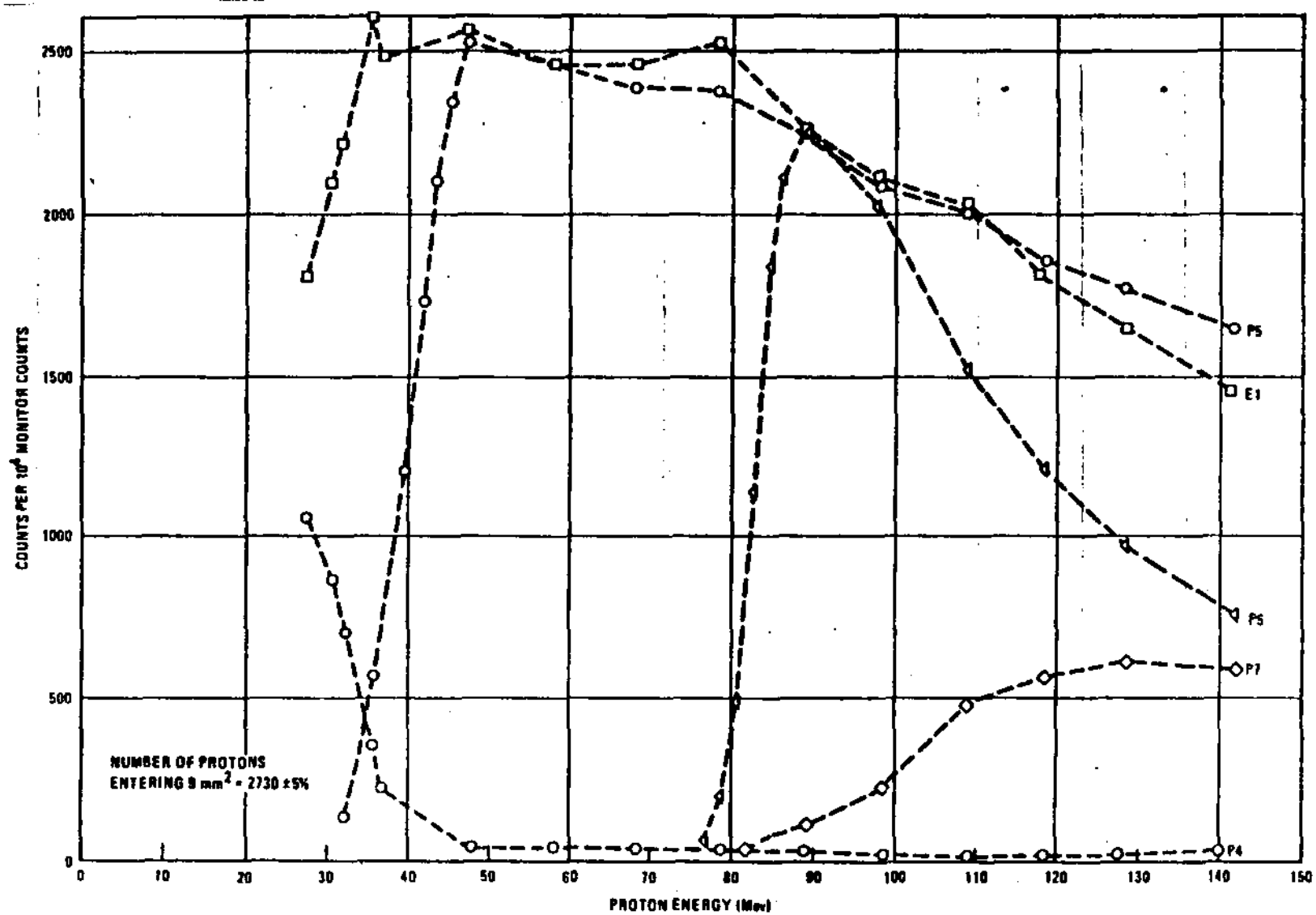

Figure 4.1 "SMS-C" Proton Calibration Data (taken directly from Ref. 1.10, Figure 16).

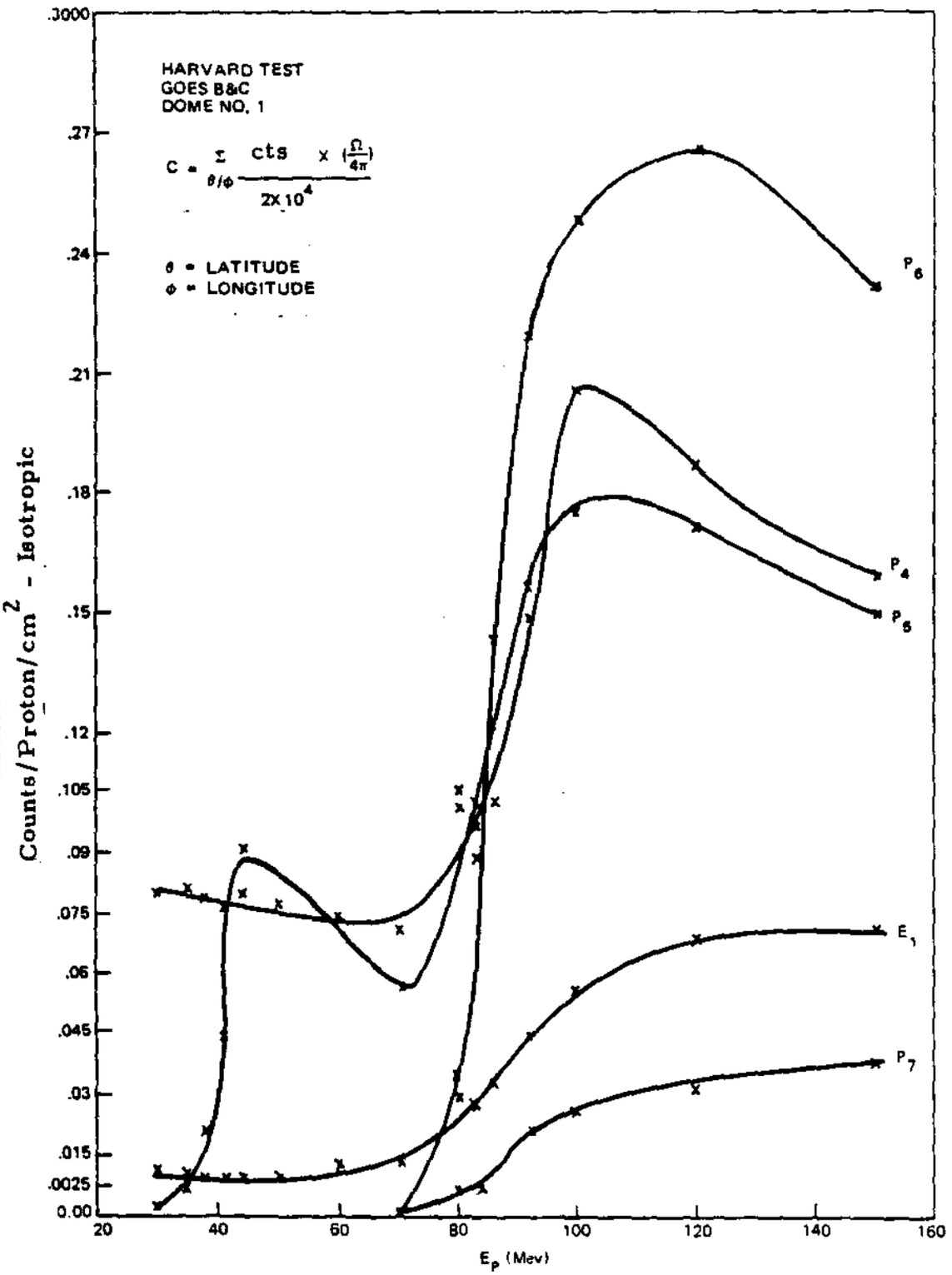

Figure 4.2 GOES B, C Proton Calibration Data (taken directly from Ref. 1.11, Figure 21).

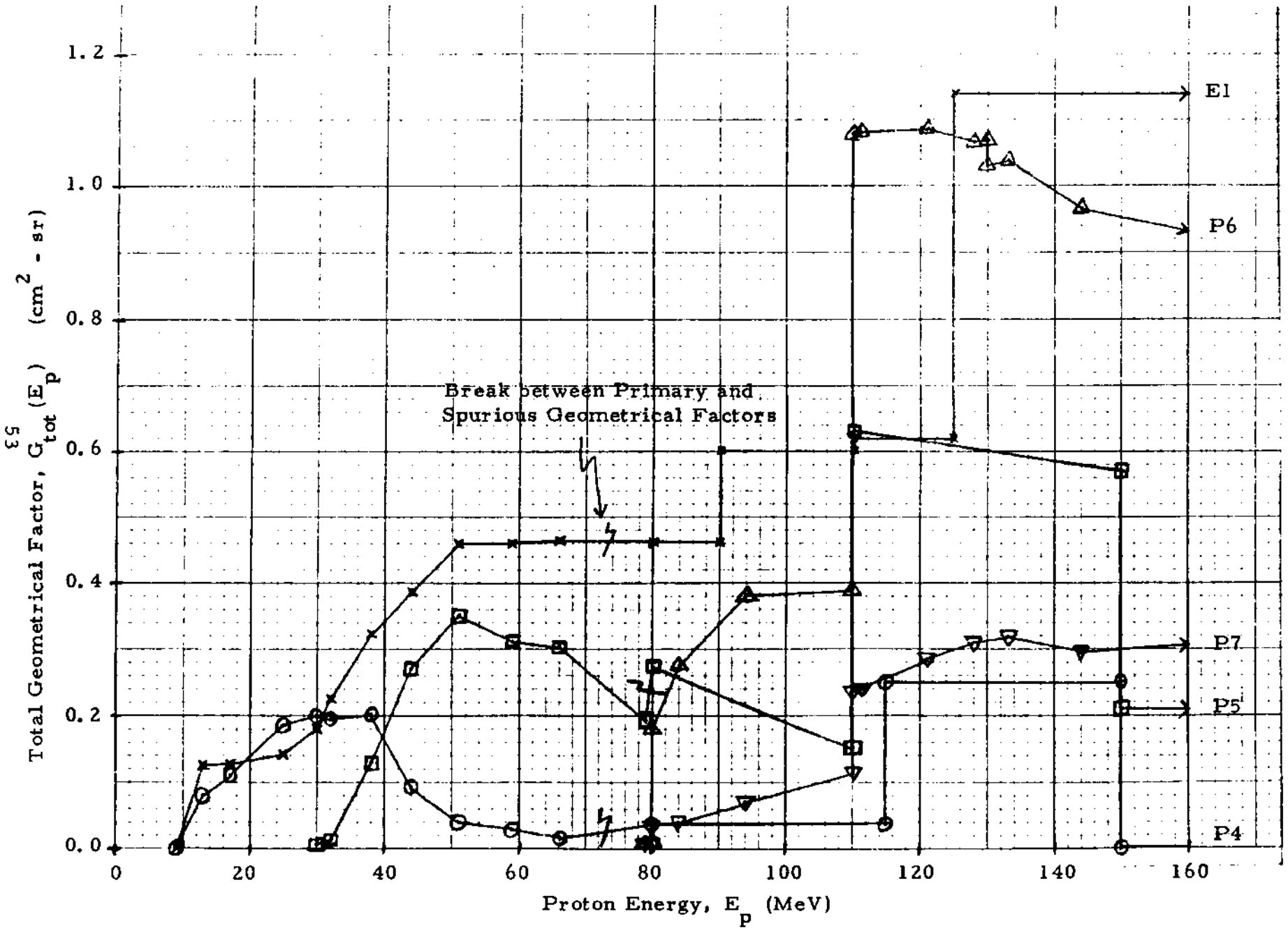

Figure 4.3 Total Geometrical Factors for Protons of the GOES D, E, F DOMEs

(penetration of the tungsten shield) in Figure 4. 3. From Figure 4. 3, it is seen that all DOME geometrical factors are at least 0. 2 cm^2-sr in the primary energy ranges for all channels, and thus meet that requirement. The overall response of the new design DOME detectors is similar to the response of the earlier design DOMEs, and within the limitations afforded by a finite amount of shielding material, provides the energy bin response of the specifications.

The DOME proton channels all have a significant response to high energy protons, in addition to the primary geometrical factor. This is shown clearly in the response curves of Figures 4. 2 and 4. 3. It is impossible to eliminate this high energy "spurious" response without the use of totally unacceptable amounts of shielding for satellite-borne detectors. However, solar flare proton spectra generally decrease rapidly with energy above a few MeV, so the effective response of the DOME channels is more nearly equal to the primary geometrical factor. The only exceptions are the high energy P6, P7 and A6 channels since for them the primary and spurious energy ranges are quite close in energy, but because they are high energy channels, there is no important shift in the effective channel response. The DOME units will thus generally respond to the approximate primary energy range for most of the duration of a solar proton event.

5. ACKNOWLEDGEMENTS

The experimental work at Brookhaven National Laboratory was carried out as part of Experiment #188. We are pleased to acknowledge the authorization of time for this experiment by the Program Advisory Committee, whose Chairman was Dr. J. Weneser at the time of this work. Much needed assistance at the Tandem Van de Graaff was provided by Dr. Ott C. Kistner, User Liaison, Mr. George Hummer, and other members of the operating staff, to whom we express sincere appreciation.

The work at the Harvard Cyclotron was carried out with the able assistance of Dr. Robert Schneider, Dr. Andy Kohler, and the other members of the staff.

Mr. Robert Varga and Mr. Dennis Padrick of Hughes Aircraft Company monitored the overall work and participated in data taking at the two accelerator facilities. Their help is very much appreciated.

REFERENCES

1.1 Bichsel, H. and C. Tschalaer, A Range-Energy Table for Heavy Particles in Silicon, Nuc. Data A, 3, 343 - 360 (1967).

1.2 Janni, J.F., Calculations of Energy Loss, Range, Pathlength, Straggling, Multiple Scattering, and the Probability of Inelastic Nuclear Collisions for 0.1 To 1,000 - MeV Protons. AFWL-TR-65-150 (1966).

1.3 Hill, C.W., W.B. Ritchie, and K.M. Simpson, Data Compilation and Evaluation of Space Shielding Problems, Vol. I, ER7777, N66-15586 (1966).

1.4 Berger, M.J., and S.M. Seltzer, Tables of Energy Losses and Ranges of Electrons and Positrons, NASA SP-3012 (1964).

1.5 Berger, M.J., and S.M. Seltzer, Additional Stopping Power and Range Tables for Protons, Mesons, and Electrons, NASA SP-3036 (1966).

1.6 Hanser, F.A., and B. Sellers, "Measurement of Totally Depleted Silicon Solid State Detector Thickness by X-Ray Attenuation", Rev. Sci. Instrum. 45, 226 - 231 (1974).

1.7 GOES D, E and F PROGRESS REPORT, EPS Tandem Van de Graaff Calibration Work Data Report #1, PANA-GOESC-PR1 (15 August 1978).

1.8 GOES D, E and F PROGRESS REPORT, EPS Tandem Van de Graaff Calibration Work Data Report #2, PANA-GOESC-PR2 (25 September 1978).

1.9 GOES D, E and F PROGRESS REPORT, Energetic Particle Sensor Telescope Calibration Work, PANA-GOESP-CR2 (16 November 1979).

1.10 Rinehart, M.C., SMS - A, B, C EPS Calibration, Philco - Ford Corporation, 3G4600-74-079, Rev. A, SMS-PCC-6252 (29 March 1974).

1.11 Nuclear Calibrations for the GOES B & C EPS, 3G9300-76-094, GOES-PCC-549 (12 August 1976).

2.1 Hanser, F.A., B. Sellers, and P.R. Morel, A Proton-Alpha Particle Detector for Use in Satellites, AFCRL-TR-73-0144, AD760 147 (1973).

2.2 Berger, M. J., S. M. Seltzer, S. E. Chappell, J. C. Humphreys, and J. W. Motz, Response of Silicon Detectors to Monoenergetic Electrons with Energies Between 0.15 and 5.0 MeV, Nucl. Instr. and Meth. 69, 181 - 193 (1969).

2.3 Seltzer, S. M., and M. J. Berger, Transmission and Reflection of Electrons by Foils, Nucl. Instr. and Meth. 119, 157 - 179 (1974).

2.4 Hogan, O. H., P. E. Zigman, and J. L. Mackin, Beta Spectra II. Spectra of Individual Negatron Emitters, USNRDL-TR-802 (16 December 1964).